

1 **Visibility-derived aerosol optical depth over global land from 1980 to** 2 **2021**

3 Hongfei Hao¹, Kaicun Wang², Chuanfeng Zhao³, Guocan Wu¹, Jing Li³

4 ¹Global Change and Earth System Science, Faculty of Geographical Science, Beijing Normal
5 University, Beijing 100875, China

6 ²Institute of Carbon Neutrality, Sino French Institute of Earth System Science, College Urban and
7 Environmental Sciences, Peking University, Beijing 100871, China

8 ³Institute of Carbon Neutrality, Department of Atmospheric and Oceanic Sciences, School of
9 Physics, College Urban and Environmental Sciences, Peking University, Beijing 100871, China

10 *Corresponding Author: Kaicun Wang (kcwang@pku.edu.cn)*

11 **Abstract**

12 Long-term and high spatial resolution aerosol optical depth (AOD) data are essential for climate
13 change detection and attribution. Global ground-based AOD observations are sparsely distributed,
14 and satellite AOD retrievals have a low temporal frequency, as well low accuracy before 2000 over
15 land. In this study, AOD is derived from hourly visibility observations collected at more than 5000
16 meteorological stations over global land from 1980 to 2021. The AOD retrievals of the Moderate
17 Resolution Imaging Spectroradiometer (MODIS) onboard the Aqua Earth observation satellite are
18 used to train the machine learning model, and the ERA5 reanalysis boundary layer height is used to
19 convert the surface visibility to AOD. Comparisons with independent datasets show that the
20 predicted AOD has correlation coefficients of 0.55 with AERONET ground observations at daily
21 time scale. The correlation coefficients are higher at monthly and annual scales, which are 0.61 for
22 the monthly and 0.65 for the annual, respectively. The visibility-derived AOD at station scale is
23 gridded into a 0.5° grid by ordinary kriging interpolation. The mean visibility-derived AOD over
24 the global land (-60°N-85°N), the Northern Hemisphere, and the Southern Hemisphere are 0.161,
25 0.158, and 0.173, with a trend of -0.0026/10a, -0.0018/10a, and -0.0059/10a from 1980 to 2021. For
26 the regional scale, the mean (trend) of AOD are 0.145 (-0.0041/10a), 0.139 (-0.0021/10a), 0.131 (-
27 0.0009/10a), 0.153 (-0.0021/10a), 0.192 (-0.0100/10a), 0.275 (-0.0008/10a), 0.177 (-0.0096/10a),
28 0.127 (-0.0081/10a), 0.177 (-0.0003/10a), 0.222 (-0.0000/10a), 0.232 (0.0071/10a), and 0.255
29 (0.0096/10a) in Eastern Europe, Western Europe, Western North America, Eastern North America,
30 Central South America, Western Africa, Southern Africa, Australia, Southeast Asia, Northeast Asia,
31 Eastern China, and India. The visibility-derived AOD at station and grid scales over global land
32 from 1980 to 2021 are available at National Tibetan Plateau / Third Pole Environment Data Center
33 (<https://doi.org/10.11888/Atmos.tpsc.300822>) (Hao et al., 2023).

34 How to cite. Hao, H., Wang, K., C. Zhao, Wu, G., J. Li (2023). Visibility-derived aerosol optical
35 depth over global land (1980-2021). National Tibetan Plateau / Third Pole Environment Data
36 Center. <https://doi.org/10.11888/Atmos.tpsc.300822>.

37 **1 Introduction**

38 Atmospheric aerosols are composed of solid and liquid particles suspended in the atmosphere.
39 Aerosol particles are directly emitted into the atmosphere or formed through gas-particle
40 transformation (Calvo et al., 2013), with diverse shapes and sizes (Fan et al., 2021), optical
41 properties, and components (Liao et al., 2015; Zhang et al., 2020; Li et al., 2022). Most atmospheric
42 aerosols are concentrated in the troposphere, especially in the boundary layer (Liu et al., 2022), with
43 a high concentration near emission sources (Kulmala et al., 2004) , and a small portion are
44 distributed in the stratosphere. Atmospheric aerosols severely impact the atmospheric environment
45 and human health. They deteriorate air quality, reduce visibility, and cause other environmental
46 issues (Wang et al., 2012; Boers et al., 2015). They impair human health or other organisms'
47 conditions by increasing cardiovascular and respiratory disease incidence and mortality rates (Chafe
48 et al., 2014; Yang et al., 2022). The Global Burden of Disease shows that global exposure to ambient
49 PM_{2.5} (particulate matter suspended in air with an aerodynamic diameter of less than 2.5
50 micrometers) resulted in 0.37 million deaths and 9.9 million disability-adjusted life years (Chafe et
51 al., 2014).

52 Aerosols are inextricably linked to climate change. Atmospheric aerosols alter the Earth's energy
53 budget and then affect the climate (Li et al., 2022). They cool the surface and heat the atmosphere
54 by scattering and absorbing solar radiation (Forster et al., 2007; Chen et al., 2022). Aerosols, such
55 as black carbon and brown carbon, also absorb solar radiation (Bergstrom et al., 2007), heat the
56 local atmosphere and suppress or invigorate convective activities (Ramanathan et al., 2001; Sun and
57 Zhao, 2020). Aerosols also alter the optical properties and life span of clouds (Albrecht, 1989).
58 Atmospheric aerosols strongly affect regional and global short-term and long-term climates through
59 direct and indirect effects (Mceill, 2017).

60 Tropospheric aerosols are considered as the second largest forcing factor for global climate change
61 (Li et al., 2022), and they reduce the warming due to greenhouse gases by -0.5°C (Ipcc, 2021).
62 However, aerosols are also regarded as the largest contributor to quantifying the uncertainty of
63 present-day climate change (Ipcc, 2021). The uncertainties are caused by the deficiencies of the
64 global descriptions of aerosol optical properties (such as scattering and absorption) and
65 microphysical properties (such as size and component), and the impact on cloud and precipitation,
66 further affecting the estimation of aerosol radiative forcing (Lee et al., 2016; Ipcc, 2021). Therefore,
67 sufficient aerosol observations are crucial. In aerosol measurements, aerosol optical depth (AOD)
68 is often used to describe its column properties, which represents the vertical integration of aerosol
69 extinction coefficients. AOD is an important physical quantity for estimating the content,
70 atmospheric pollution and climatology of aerosols (Zhang et al., 2020).

71 AOD data usually from ground-based and satellite-borne remote sensing observations. They have
72 both advantages and disadvantages. Ground-based lidar observation is an active remote sensing
73 technology. Lidar generally emits laser and receives backscattered signals to invert the extinction
74 coefficient of aerosols at different heights (Klett, 1985). By using the depolarization ratio, the type
75 of aerosol, such as fine particles or dust, can be distinguished (Bescond et al., 2013). The AOD
76 within a certain height can be calculated by integrating the extinction coefficients; however,
77 scattering signals are usually not received near the ground, leading to blind spots (Singh et al., 2019).

78 At present, there are many ground-based lidar worldwide and regional networks, which provides
79 important support of vertical changes in aerosols, such as the NASA Micro-Pulse Lidar Network
80 (MPLNET) in the early 1990s (Welton et al., 2002), the European Aerosol Research Lidar Network
81 (EARLINET) since 2000 (Bösenberg and Matthias, 2003), the Latin American Lidar Network
82 (LALINET) since 2013 (Guerrero-Rascado et al., 2016).

83 Ground-based remote sensing observations supply aerosol loading data (such as AOD), by
84 measuring the attenuation of radiation from the top of the atmosphere to the surface (Holben et al.,
85 1998). This type of observation mainly uses weather-resistant automatic sun and sky scanning
86 spectral radiometers to retrieve optical and microphysical aerosol properties (Che et al., 2014). The
87 Aerosol Robotic Network (AERONET) is a popular global network composed of NASA and
88 multiple international partners that provides high-quality and high-frequency aerosol optical and
89 microphysical properties under various geographical and environmental conditions (Holben et al.,
90 1998; Dubovik et al., 2000). The AERONET observations are extensively used to validate satellite
91 remote sensing observations and model simulations, as well as climatology study (Dubovik et al.,
92 2002b). There are many regional networks of sun photometers, such as the Maritime Aerosol
93 Network (MAN), which use a handheld sun photometer to collect data over the ocean and is merged
94 into AERONET (Smirnov et al., 2009), the China Aerosol Robot Sun Photometer Network
95 (CARSNET) (Che et al., 2009), the Canadian sub-network of AERONET (AEROCAN) (Bokoye et
96 al., 2001), Aerosol characterization via Sun photometry: Australian Network (AeroSpan)
97 (Mukkavilli et al., 2019), and the sky radiometer network (SKYNET) in Asia and Europe (Kim et
98 al., 2004; Nakajima et al., 2020). Another very valuable global network is the NOAA/ESRL
99 Federated Aerosol Network (FAN), which uses integrated nephelometers distinct from sun
100 photometers, mainly located in remote areas, providing background aerosol properties over 30 sites
101 (Andrews et al., 2019).

102 Satellite remote-sensing is a space-based method that can provide aerosol properties worldwide.
103 With the development of satellite remote sensing technology since 1970s, aerosol distributions can
104 be extracted with the advantage of sufficient real-time and global coverage from multiple satellite
105 sensors (Kaufman and Boucher, 2002; Anderson et al., 2005). The Advanced Very High Resolution
106 Radiometer (AVHRR) is the earliest sensor used for retrieving AOD over ocean (Nagaraja Rao et
107 al., 1989). The Moderate Resolution Imaging Spectroradiometer (MODIS), on board the Terra
108 (launched in 1999) and Aqua (launched in 2002) satellites is a popular sensor with 36 channels,
109 which have been used for AOD retrieval over both ocean and land based on the Dark Target and the
110 Deep Blue algorithms (Remer et al., 2005; Levy et al., 2013). The latest MODIS AOD data version
111 is the Collection 6.1, which provides global AOD over 20 years (Wei et al., 2019). There are also
112 many other satellite sensors that can be used to retrieve AOD, such as the Polarization and
113 Directionality of the Earth's Reflectances (POLDER) during 1996-1997, 2003 and 2004-2013
114 (Deuzé et al., 2000), Sea-viewing Wide Field-of-view Sensor (SeaWiFS) during 1997-2007
115 (O'reilly et al., 1998), the Multi-angle Imaging Spectroradiometer (MISR) on Terra since 1999
116 (Diner et al., 1998). The Cloud-Aerosol Lidar with Orthogonal Polarization (CALIOP) has also
117 derived aerosols in the vertical direction since 2006 (Winker et al., 2009).

118 These measurements provide important data for studying the global and regional spatiotemporal
119 variabilities and climate effect of aerosols. However, ground-based remote sensing observations
120 only provide aerosol properties with low spatial coverage. There were only about 150 ground

121 stations worldwide in 2002 and even fewer sites were available for climate analysis (Holben et al.,
122 1998; Chu et al., 2002), which limited aerosol climate research by spatial coverage (Bright and
123 Gueymard, 2019). Satellite remote sensing overcomes the limitations of spatial coverage. The
124 AVHRR has been used to retrieve AOD since 1980, but it is limited by a few channel number, low
125 spatial resolution, and insufficient validation through ground-based observations before 2000 (Hsu
126 et al., 2017). Many studies have only investigated the trends and distributions of aerosols after 2000
127 (Bösenberg and Matthias, 2003; Winker et al., 2013; Xia et al., 2016; Tian et al., 2023), because of
128 the lack of long-term and global cover AOD products, which is the bottleneck for aerosol climate
129 change detection and attributions.

130 To overcome these limitations and enrich aerosol data, alternative observation data could be utilized
131 to derive AOD. Atmospheric horizontal visibility is a suitable alternative (Wang et al., 2009; Zhang
132 et al., 2020), because it has the advantages of the long-term records with a large number of stations
133 worldwide.

134 Atmospheric visibility is a physical quantity that describes the transparency of the atmosphere
135 through manual and automatic observations, and the automatic observations of visibility usually
136 measure atmospheric extinction (scattering coefficient and transmissivity). Koschmieder (1924)
137 first proposed the relationship between the meteorological optical range and the total optical depth.
138 Elterman (1970) further established a formula between AOD and visibility by assuming an
139 exponential decrease in aerosol concentration with altitude, considering the extinction of molecules
140 and ozone to analyze air pollution, which called the Elterman model. Qiu and Lin (2001) corrected
141 the Elterman model by considering the influence of water vapor and used two water vapor pressure
142 correction coefficients to retrieve AOD of 16 stations in China in 1990. Wang et al. (2009) analyzed
143 the trend of AOD using visibility-based retrievals from 1973 to 2007 over land. Lin et al. (2014)
144 retrieved the AOD in eastern China in 2006 using visibility and aerosol vertical profiles provided
145 by GEOS-Chem. Wu et al. (2014) and Zhang et al. (2017) parameterized the constants in the
146 Elterman model and use satellite retrieved AOD to solve the parameters in the models at different
147 stations, to retrieve the long-term AOD in China.

148 Zhang et al. (2020) reviewed the methods of visibility retrieval of AOD, indicating that visibility-
149 based retrieval of AOD can compensate for the shortcomings of long-term aerosol observation data.
150 Simultaneously, various parameters, such as station altitude, consistency of visibility data, water
151 vapor and aerosol vertical profiles (scale height), were discussed with modified suggestions
152 proposed. These studies have enriched AOD data regionally. These studies have enriched aerosol
153 data in some extent. At present, there are very few studies on global visibility-retrieved AOD and to
154 analyze climatology of aerosols.

155 The two physical quantities of visibility and AOD have both connections and differences, making it
156 challenging to retrieve AOD from visibility. Visibility represents the maximum horizontal visible
157 distance near the surface, while AOD represents the total vertical attenuation of solar radiation by
158 aerosols. The visibility of automatic observation is dependent on the local horizontal atmospheric
159 extinction (Noaa et al., 1998). Visibility has not a simple linear relationship with meteorological
160 factors. The vertical structure of aerosols is the greatest challenge to obtain, as it is not a simple
161 hypothetical curve in complex terrain and circulation conditions (Zhang et al., 2020). These
162 limitations make it more complex to derive AOD. Machine learning methods can effectively address

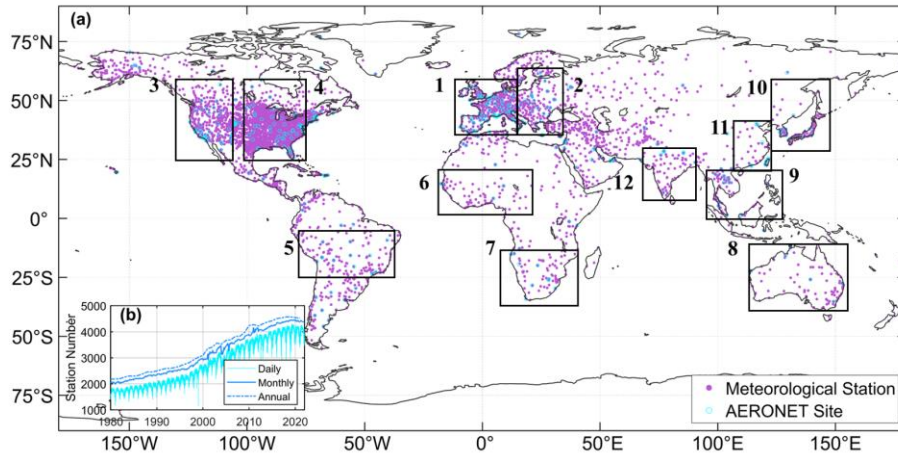
163 complex nonlinear relationships between variables and have been widely applied in remote sensing
164 and climate research fields. Li et al. (2021) used the random forest method to predict $PM_{2.5}$ in Iraq
165 and Kuwait based on satellite AOD during 2001-2018. Kang et al. (2022) applied LightGBM and
166 random forest to estimate AOD over East Asia, and the results showed a consistency with
167 AERONET. Dong et al. (2023) derived aerosol single scattering albedo from visibility and satellite
168 AOD over 1000 global stations. Hu et al. (2019) used a deep learning method to retrieve horizontal
169 visibility from MODIS AOD. These studies have confirmed the ability of machine learning to
170 effectively solve complex relationships among variables. And previous studies are mostly
171 conducted at the regional or national scale, and few studies at the global scale. Thus, it is feasible to
172 derive AOD from atmospheric visibility over global land by using the machine learning method.

173 In this study, we propose a machine learning method to derive AOD, where satellite AOD is the
174 target value, and visibility and other related meteorological variables are the predictors. We explain
175 the robustness of the model, validate the model's predictions using independent ground-based AOD,
176 satellite retrievals and reanalysis AOD, and analyze the mean and trend of AOD across land and
177 regions. Two datasets of long-term high-resolution AOD are generated. The Section 2 introduces
178 the data and method. The Section 3 is the evaluation and validation of the visibility-derived AOD,
179 and the distribution and trends are discussed at global and regional scales. The Section 5 presents
180 the conclusions. This study is dedicated to supporting the research of aerosols in climate change
181 detection and attribution.

182 **2 Data and method**

183 **2.1 Study area**

184 The study area is global land. A total of 5032 meteorological stations and 395 AERONET sites are
185 selected in this study, shown in Figure 1. Twelve regions are selected for special analysis, including
186 Eastern Europe, Western Europe, Western North America, Eastern North America, Central South
187 America, Western Africa, Southern Africa, Australia, Southeast Asia, Northeast Asia, Eastern China,
188 and India. The time range of the study is from 1980 to 2021, during which the records of
189 meteorological stations are sufficient with a uniform spatial distribution. As shown in Figure 1, the
190 daily records have exceeded 1500 stations, and monthly and annual records have exceeded 2000
191 during 1980-1990. After 2000, monthly records have reached 3000, which is the foundation of
192 gridding AOD.



193

194 **Figure 1:** Study area (a) and the meteorological station number (b) with daily, monthly, and annual
 195 records. The number of meteorological stations (filled circles) is 5032. The number of AERONET
 196 sites (empty circles) is 395. The box regions of labelled with number 1-12 are Eastern Europe,
 197 Western Europe, Western North America, Eastern North America, Central South America, Western
 198 Africa, Southern Africa, Australia, Southeast Asia, Northeast Asia, Eastern China, and India.

199 2.2 Meteorological data

200 The ground hourly data from 1980 to 2021 is collected from 5032 automated meteorological stations
 201 of airports over land. Automated surface observations reduce errors associated with human
 202 involvement in data collection, processing, and transmission. The data can be downloaded at
 203 <https://mesonet.agron.iastate.edu/ASOS>. The data is extracted from the Meteorological Terminal
 204 Aviation Routine Weather Report (METAR). The World Meteorological Organization (WMO) sets
 205 guidelines for METAR reports, including report format, encoding, observation instruments and
 206 methods used, data accuracy, and consistency. These requirements ensure consistency and
 207 comparability of METAR reports globally. International regulations can be referenced at
 208 <https://community.wmo.int/en/implementation-areas-aeronautical-meteorology-programme>.
 209 Among them, over 1,000 stations belong to the Automated Surface Observing System (ASOS), and
 210 others are sourced from airport reports around the world.

211 The daily average visibility is calculated using harmonic mean. Experiments have found that
 212 harmonic average visibility can better detect the weather phenomena than arithmetic average
 213 visibility (Noaa et al., 1998). The visibility is calculated using the extinction coefficient, which is
 214 directly proportional to the reciprocal of visibility (Wang et al., 2009). Harmonious average
 215 visibility can capture the process of visibility decline more quickly. Therefore, daily visibility will
 216 have greater representativeness:

$$217 \quad V = n / \left(\frac{1}{V_1} + \frac{1}{V_2} + \dots + \frac{1}{V_n} \right), \quad (1)$$

218 where V is the harmonic mean visibility, $n = 24$ for the daily visibility, and V_1, V_2, \dots, V_n are the
 219 individual hourly visibility.

220 In addition to hourly visibility (VIS), other variables closely related to aerosol properties are selected,

221 including relative humidity (RH), dew point temperature (DT), temperature (TMP), wind speed
222 (WS) and sea-level pressure (SLP). Temperature affects atmospheric stability and the rate of
223 secondary particle formation, and humidity influences the size and hygroscopic growth, and wind
224 speed and pressure significantly impact the transport and deposition. Sky conditions (cloud amount)
225 and hourly precipitation are also selected to remove the records of extensive cloud cover and
226 precipitation.

227 We processed the data as follows. The records with high missing value ratio are eliminated (Husar
228 et al., 2000). When over 80% overcast or fog, the records of sky conditions are eliminated, though
229 such situations occur less than 1% of the time over land (Remer et al., 2008). The records with 1-
230 hour precipitation greater than 0.1 mm are eliminated. We calculate the temperature dew point
231 difference (dT). The low visibility records under “blowing snow” weather are eliminated at high
232 latitude region ($> 65^{\circ}\text{N}$), when wind speed is great than 4.5m/s (Husar et al., 2000). When the RH
233 is greater than 90%, it is impossible to distinguish whether it is fog or haze, or both, and even
234 precipitation. The records with RH greater than or equal to 90% are eliminated. When the RH is less
235 than 30%, the dilution effect of aerosols is very low or even negligible. When RH is between 30%
236 and 90%, visibility is converted to dry visibility (Yang et al., 2021c):

$$237 \quad \mathbf{VISD} = \mathbf{VIS}/(\mathbf{0.26} + \mathbf{0.4285} * \mathbf{log}(100 - \mathbf{RH})), \quad (2)$$

238 where VISD is the dry visibility.

239 Daily average of variables is calculated by at least 3 hourly records.

240 **2.3 Boundary layer height**

241 The hourly boundary layer height (BLH) from 1980 to 2021 is available from the Fifth Generation
242 reanalysis of the European Medium-Range Weather Forecast Center (ERA5) with a resolution of
243 $0.25^{\circ} \times 0.25^{\circ}$ (<https://cds.climate.copernicus.eu>), which is the successor of ERA-Interim and has
244 undergone various improvements (Hersbach et al., 2020). The atmospheric boundary layer is the
245 layer closest to the Earth’s surface and exhibits complex turbulence activities, and its height
246 undergoes significant diurnal variation. The effects of the boundary layer on aerosols are mainly
247 manifested in vertical distribution, concentration changes, transport, and deposition (Ackerman et
248 al., 1995). The characteristics and variations in the boundary layer play a crucial role in regulating
249 and adjusting the distribution of atmospheric aerosols. The boundary layer height serves as an
250 approximate measure of the scale height for aerosols (Zhang et al., 2020).

251 Compared to observations of 300 stations over world from 2012 to 2019, the BLH of ERA5 was
252 underestimated by 131.96m. Compared with the underestimated MERRA-2 (166.35m), JRA-55
253 (351.49m), and NECP-2 (420.86m), the BLH of ERA5 was closest to the observations (Guo et al.,
254 2021). The BLH hourly data is temporally and spatially matched with the meteorological data before
255 calculating the daily average.

256 Because the inverse of visibility is proportional to the extinction coefficient and positively related
257 to AOD (Wang et al., 2009), we calculated the reciprocal of visibility (VISI) and the reciprocal of
258 dry visibility (VISDI). Due to the influence of boundary layer height on the vertical distribution of
259 particles (Zhang et al., 2020), we calculated the product (VISDIB) of the reciprocal of dry visibility
260 and BLH. Therefore, the Predictor (Figure 2) is composed of 11 variables (TMP, Td, dT, RH, SLP,
261 WS, VIS, BLH, VISI, VISDI, and VISDIB).

262 **2.4 MODIS AOD products**

263 Satellite daily AOD is available from the Moderate Resolution Imaging Spectroradiometer (MODIS)
264 Level 3 Collection 6.1 AOD products of the Aqua (MYD09CMA) satellite from 2002 to 2021 and
265 Terra (MOD09CMA) satellite from 2000 to 2021 with a spatial resolution of $0.05^\circ \times 0.05^\circ$ at a
266 wavelength of 550 nm (<https://ladsweb.modaps.eosdis.nasa.gov>). MOD/MYD09 has a higher
267 spatial resolution than MOD/MYD08 ($1^\circ \times 1^\circ$), which may result in a greater difference in AOD
268 values and reduce the proximity ratio to match the visibility-derived AOD at station scale. Terra
269 (passing approximately 10:30 am local time) and Aqua (passing approximately 1:30 pm local time)
270 were successfully launched in December 1999 and May 2002, respectively.

271 MODIS, carried on the Terra and Aqua satellites is a crucial instrument in the NASA Earth
272 Observing System program, which is designed to observe global biophysical processes
273 (Salomonson et al., 1987). The 2,330 km-wide swath of the orbit scan can cover the entire globe
274 every one to two days. MODIS has 36 channels and more spectral channels than previous satellite
275 sensors (such as AVHRR). The spectral range from 0.41 to $15\mu\text{m}$ representing three spatial
276 resolutions: 250 m (2 channels), 500 m (5 channels), and 1 km (29 channels). The aerosol retrieval
277 algorithms use seven of these channels ($0.47\text{--}2.13\mu\text{m}$) to retrieve aerosol characteristics and uses
278 additional wavelengths in other parts of the spectrum to identify clouds and river sediments.
279 Therefore, it has the ability to characterize the spatial and temporal characteristics of the global
280 aerosol field.

281 The MODIS aerosol product actually takes use of different algorithms for deriving aerosols over
282 land and ocean. The Dark Target (DT) algorithm is applied to densely vegetated areas because the
283 surface reflectance over dark-target areas was lower in the visible channels and had nearly fixed
284 ratios with the surface reflectance in the shortwave and infrared channels (Levy et al., 2007; Levy
285 et al., 2013). The Deep Blue (DB) algorithm was originally applied to bright land surfaces (such as
286 deserts), and later extended to cover all cloud-free and snow-free land surfaces (Hsu et al., 2006;
287 Hsu et al., 2013). MODIS Collection 6.1 aerosol product was released in 2017, incorporating
288 significant improvements in radiometric calibration and aerosol retrieval algorithms.

289 The expected errors are $\pm (0.05 \pm 15\%)$ for the DT retrievals over land. Higher spatial coverage is
290 observed in August and September, reaching 86-88%. During December and January, due to the
291 presence of permanent ice and snow cover in high-latitude regions of the Northern Hemisphere, the
292 spatial coverage is 78-80%. Thus, challenges remain in retrieving AOD values in high-latitude
293 regions (Wei et al., 2019). However, visibility observations are available in high-latitude regions,
294 thereby partially addressing the lack in these regions. In this study, the Terra and Aqua MODIS AOD
295 are temporally and spatially matched with the meteorological stations. Aqua MODIS AOD is used
296 as the Target, when training the model, and Terra MODIS AOD is used in the evaluation and
297 validation of the model results, as shown in the flowchart (Figure 2).

298 **2.5 Ground-based AOD**

299 Ground-based 15-minute AOD data are available from the Aerosol Robotic Network (AERONET)
300 Version 3.0 Level 2.0 product at 395 sites (Figure 1), which can be downloaded from
301 <https://aeronet.gsfc.nasa.gov>. The AERONET program is a federation of ground-based remote
302 sensing aerosol networks established by NASA and PHOTONS, including many subnetworks (such
303 as AeroSpan, AEROCAN, NEON, and CARSNET). The sun photometer (CE-318) measures

304 spectral sun and sky irradiance in the 340-1020 nm spectral range. When the aerosol loading is low,
305 the error is significant. When the AOD at 440 nm wavelength is less than 0.2, the error is 0.01,
306 which is equivalent to the error of the absorption band in the total optical depth (Dubovik et al.,
307 2002a). The total uncertainty in AOD under cloud-free conditions is less than ± 0.01 for wavelength
308 more than 440 nm, and ± 0.02 for wavelength less than 440 nm (Holben et al., 1998). AERONET
309 has three levels of AOD products: Level 1.0 (unscreened), Level 1.5 (cloud screened), and Level
310 2.0 (cloud screened and quality assured). Compared to Version 2, the Version 3 Level 2.0 database
311 has undergone further cloud screening and quality assurance, which is generated based on Level 1.5
312 data with pre- and post-calibration and temperature adjustment and is recommended for formal
313 scientific research (Giles et al., 2019). AERONET provides AOD products at wavelengths of 440,
314 675, 870, and 1020 nm. The AOD at 440nm and the Ångström index at 440-675nm are used for
315 AOD at 550 nm not provided by AERONET, as shown in Eq. (3). AERONET AOD, as the ‘true’
316 value, is the average of at least two times within 1 hour (± 30 minutes) of Aqua transit time (Wei et
317 al., 2019):

$$318 \quad \tau_{550} = \tau_{440} \left(\frac{550}{440} \right)^{-\alpha}, \quad (3)$$

319 where τ_{440} and τ_{550} are the AOD at a wavelength of 440nm and 550 nm, and α is the Ångström
320 index.

321 The matching conditions between AERONET sites and meteorological stations are (1) a distance of
322 less than 0.5° (2) at least three years of observation. Finally, a total of 395 pairs were matched.

323 **2.6 AOD reanalysis dataset**

324 The monthly AOD (550nm) dataset of Modern-Era Retrospective Analysis for Research and
325 Applications version 2 (MERRA-2) from 1980 to 2021 is a NASA reanalysis of the modern satellite
326 era produced by NASA’s Global Modeling and Assimilation Office with a spatial resolution of
327 $0.5 \times 0.625^\circ$ (Gelaro et al., 2017), available at <https://disc.gsfc.nasa.gov>. MERRA-2 AOD uses an
328 analysis splitting technique to assimilate AOD at 550 nm. AOD observations are including (1)
329 AOD retrievals from AVHRR (1979-2002) over global ocean, (2) AOD retrievals from MODIS on
330 Terra (2000–present) and Aqua (2002–present) over global land and ocean, (3) AOD retrievals from
331 MISR (2000–2014) over bright and desert surfaces, and (4) direct AOD measurements from the
332 ground-based AERONET (1999–2014) (Gelaro et al., 2017). The monthly MERRA-2 AOD is used
333 to evaluate the model’s predictive ability before 2000 and after 2000.

334 **2.7 Decision tree regression**

335 **2.7.1 Feature selection**

336 Although a multidimensional dataset can provide as much potential information as possible for
337 AOD, irrelevant and redundant variables can also introduce significant noise in the model and
338 reduce the model’s accuracy and stability (Kang et al., 2021; Dong et al., 2023). Therefore, the F-
339 test is used to search for the optimal feature subset in the Predictor, aiming to eliminate irrelevant
340 or redundant features and select truly relevant features, which helps to simplify the model’s input
341 and improve the model’s prediction ability (Dhanya et al., 2020). The F-test is a statistical test that
342 gives an f-score($=-\log(p)$, p represents the degree to which the null hypothesis is not rejected) by

343 calculating the ratio of variances. In this study, we calculate the ratio of variance between the
344 Predictors and Target, and the features are ranked based on higher values of the f-score. A greater
345 value of f-score means that the distances between Predictors and Target are less and the relationship
346 is closer, thus, the feature is more important. We set $p=0.05$. When the score is less than $-\log(0.05)$,
347 the variable in the Predictors is not considered.

348 **2.7.2 Data balance**

349 When it is clear, the AOD value is small, the variability of AOD is small ($AOD < 0.5$), and the data is
350 concentrated near the mean value. When heavy pollution, the AOD value is large ($AOD > 0.5$). Compared
351 to clear sky, the AOD sequence will show "abnormal" large values with low frequency, which is the
352 imbalance of AOD data. When dealing with imbalanced datasets, because of the tendency of machine
353 learning algorithms to perform better on the majority class and overlook the minority class, the model
354 can be underfit (Chuang and Huang, 2023). Data augmentation techniques are commonly employed to
355 address the issue in imbalance data, which applies a series of transformations or expansions to generate
356 new training data, thereby increasing the diversity and quantity of the training data.

357 The Adaptive Synthetic Sampling (ADASYN) is a data augmentation technique specifically designed to
358 address data imbalance problem (He et al., 2008; Mitra et al., 2023). It is an extension of the Synthetic
359 Minority Over-sampling Technique (SMOTE) algorithm (Fernández et al., 2018). The goal of ADASYN
360 is to generate synthetic sample data for the minority class to increase its representation in the dataset.
361 ADASYN, which adaptively adjusts the generation ratio of synthetic samples based on the density
362 distribution of sample data, improves the dataset balance and enhances the performance of machine
363 learning models in dealing with imbalanced data.

364 The processing of imbalanced data includes (1) AOD sequences are classified into three types based on
365 percentile (0-1%, 2% -98%, 99%), (2) When the mean of the third type of AOD is greater than 5 times
366 the standard bias of the second type, it is considered an imbalanced sequence. These data, with a total
367 amount less than 5% of the sample, are imbalanced data, and (3) Then synthetic samples are generated
368 with the upper limit 10% of the samples.

369 **2.7.3 Decision tree regression model**

370 The decision tree is a machine learning algorithm based on a tree-like structure used to solve
371 classification and regression problems. We adopt the CART algorithm to construct a regression tree by
372 analyzing the mapping relationship between object attributes (Predictors) and object values (Target). The
373 internal nodes have binary tree structures with feature values of "yes" and "no". In addition, each leaf
374 node represents a specific output for a feature space. The advantages of the regression tree include the
375 ability to handle continuous features and the ease of understanding the generated tree structure (Teixeira,
376 2004; Berk, 2008). Before training the tree model, the variables (Input) are normalized to improve model
377 performance, and after prediction, the results are obtained by denormalization. The 10-fold cross-
378 validation method is employed to improve the generalization ability of the model (Browne, 2000).

379 The core problems of the regression tree need to be solved are to find the optimal split variable and
380 optimal split point. The optimal split point of Predictors is determined by the minimum MSE, which in
381 turn determines the optimal tree structure. We set $Y = [y_1, y_2, \dots, y_N]$ as the Target. We set $X =$
382 $[x_1, x_2, \dots, x_N]$ as the Predictors, $x_i = (x_i^1, x_i^2, \dots, x_i^n)$, $i = 1, 2, 3, \dots, N$, where n is the feature number, and
383 N is the length of sample. We set a training dataset as $D = [(x_1, y_1), (x_2, y_2), \dots, (x_N, y_N)]$.

384 A regression tree corresponds to a split in the feature space and the output values on the split domains.
 385 Assuming that the input space has been divided into M domains $[R_1, R_2, \dots, R_M]$ and there is a fixed
 386 output value on each R_M domain, the regression tree model can be represented as follows:

$$387 \quad f(x) = \sum_{m=1}^M c_m I(x \in R_m), m = 1, 2, \dots, M, \quad (4)$$

388 where I is the indicator function, Eq. (5):

$$389 \quad I = \begin{cases} 1, & x \in R_m \\ 0, & x \notin R_m \end{cases}, \quad (5)$$

390 When the partition of the input space is determined, the square error can be used to represent the
 391 prediction error of the regression tree for the training data, and the minimizing square error is used to
 392 solve the optimal output value on each domain. The optimal value (\widehat{c}_m) on a domain is the mean of the
 393 outputs corresponding to all input, namely:

$$394 \quad \widehat{c}_m = \text{ave}(y_i | x_i \in R_m), \quad (6)$$

395 A heuristic method is used to split the feature space in CART. After each split, all values of all features
 396 in the current set are examined individually, and the optimal one is selected as the split point based on
 397 the principle of minimum sum of the square errors. The specific step is described as follows: for the
 398 training dataset D , we recursively divide each region into two sub domains and calculate the output
 399 values of each sub domain; then, construct a binary decision tree. For example, split variable is x^j and
 400 split point is s . Then, in the domain $R_1(j, s) = [x|x^j \leq s]$ and domain $R_2(j, s) = [x|x^j > s]$, we can
 401 solve the loss function $L(j, s)$ to find the optimal j and s .

$$402 \quad L(j, s) = \sum_{x_i \in R_1(j, s)} (y_i - c_1)^2 + \sum_{x_i \in R_2(j, s)} (y_i - c_2)^2, \quad (7)$$

403 When $L(j, s)$ is the smallest, x^j is the optimal split variable and s is the optimal split point for the
 404 x^j .

$$405 \quad \min_{j, s} \left[\min_{c_1} \sum_{x_i \in R_1(j, s)} (y_i - c_1)^2 + \min_{c_2} \sum_{x_i \in R_2(j, s)} (y_i - c_2)^2 \right], \quad (8)$$

406 We use the optimal split variable x^j and the optimal split point s to split the feature space and calculate
 407 the corresponding output value.

$$408 \quad \widehat{c}_1 = \text{ave}(y_i | x_i \in R_1(j, s)), \quad \widehat{c}_2 = \text{ave}(y_i | x_i \in R_2(j, s)), \quad (9)$$

409 We traverse all input variables to find the optimal split variable x^j , forming a pair (j, s) . Divide the
 410 input space into two regions accordingly. Next, repeat the above process for each region until the stop
 411 condition is met. The regression tree is generated.

412 Therefore, the regression tree model $f(x)$ can be represented as follows:

$$413 \quad f(x) = \sum_{m=1}^M \widehat{c}_m I(x \in R_m), m = 1, 2, \dots, M, \quad (10)$$

414 2.8 Gridding method

415 Kriging is a regression algorithm to model and predict (interpolate) random processes/fields based on the
 416 covariance function, which is widely used in geo-statistics (Pebesma, 2004). Ordinary Kriging is the

417 earliest and most extensively studied form of Kriging. It is a linear estimation system applicable to any
 418 intrinsic stationary random field that satisfies the assumption of isotropy. The two key parameters of
 419 Ordinary Kriging are the semi-variogram function and the weight factors (Goovaerts, 2000). It has been
 420 widely applied in fields, such as climatology, environmental science, and agriculture (Lapen and Hayhoe,
 421 2003; Chen et al., 2010), due to high accuracy, stability, and insensitivity to data shape and distribution.
 422 This study utilizes area-weighted ordinary kriging algorithm to estimate the unknown values of AOD at
 423 specific locations to generate gridded AOD. The longitude range is between -179.5° E and 180 °E, the
 424 latitude range is between -60 °N and 85 °N, and the spatial resolution is 0.5 °*0.5 °.

425 Kriging variance represents the spatial correlation between different points, which is calculated by the
 426 semi variogram function (Goovaerts, 2000). Kriging variance is used to assess the spatial uncertainty of
 427 interpolation results, indicating the difference between predicted and true values. A higher kriging
 428 variance indicates fewer neighboring points and greater uncertainty, while a lower variance implies less
 429 uncertainty. To quantify the uncertainty of interpolation results, we provide the width of the confidence
 430 interval under the 95% confidence level based on kriging variance (Van Der Veer et al., 2009).

431 2.9 Evaluation metrics

432 Evaluation metrics, including Root Mean Squared Error (RMSE), Mean Absolute Error (MAE) and
 433 Pearson Correlation Coefficient (R), are used to measure the performance and accuracy of the model and
 434 gridded results.

$$435 \quad \mathbf{RMSE} = \sqrt{\frac{1}{n} \sum_{i=1}^n (y_i - \hat{y}_i)^2}, \quad (11)$$

$$436 \quad \mathbf{MAE} = \frac{1}{n} \sum_{i=1}^n |y_i - \hat{y}_i|, \quad (12)$$

$$437 \quad \mathbf{R} = \frac{\sum_{i=1}^n (y_i - \bar{y})(\hat{y}_i - \bar{\hat{y}})}{\text{sqrt}(\sum_{i=1}^n (y_i - \bar{y})^2 \sum_{i=1}^n (\hat{y}_i - \bar{\hat{y}})^2)}, \quad (13)$$

438 where y_i and \bar{y} are the predicted value and the average of the predicted values. \hat{y}_i and $\bar{\hat{y}}$ are
 439 the target and the average of the target. $i = 1, 2, \dots, n$. n is the length of sample.

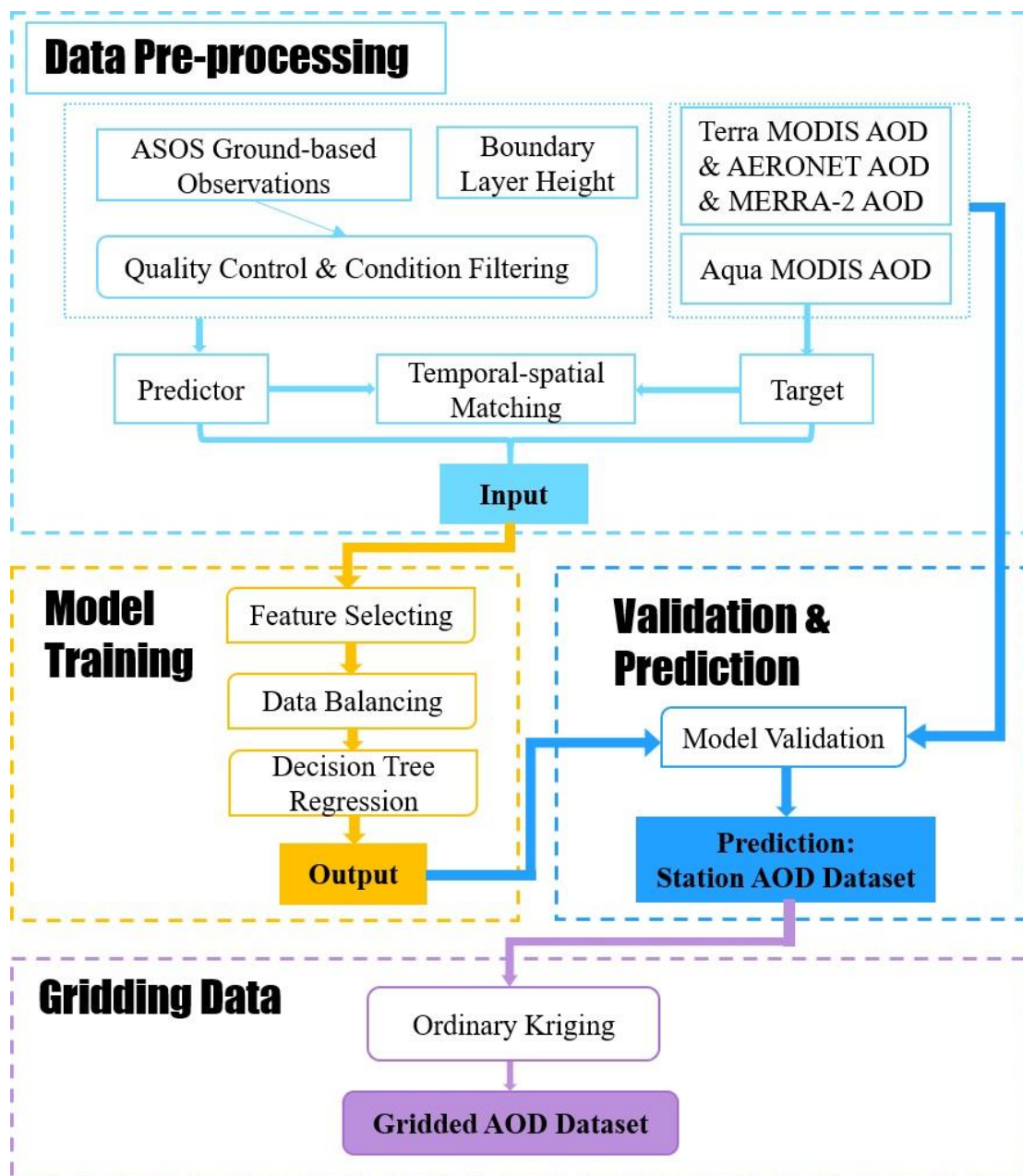
440 The expected error (EE) is used to evaluate the AOD derived from visibility.

$$441 \quad \mathbf{EE} = \pm(0.05 + 0.15 * \tau_{true}), \quad (14)$$

442 where τ_{true} is the AOD at 550 nm from AERONET, satellite and reanalysis datasets.

443 The width of 95% confidence interval (CI) is calculated from the kriging variance (s^2) (Van Der Veer et
 444 al., 2009) :

$$445 \quad \mathbf{95\% \ CI} = 1.96 * \sqrt{s^2}, \quad (15)$$



446

447 **Figure 2:** Flowchart for deriving aerosol optical depth (AOD).

448

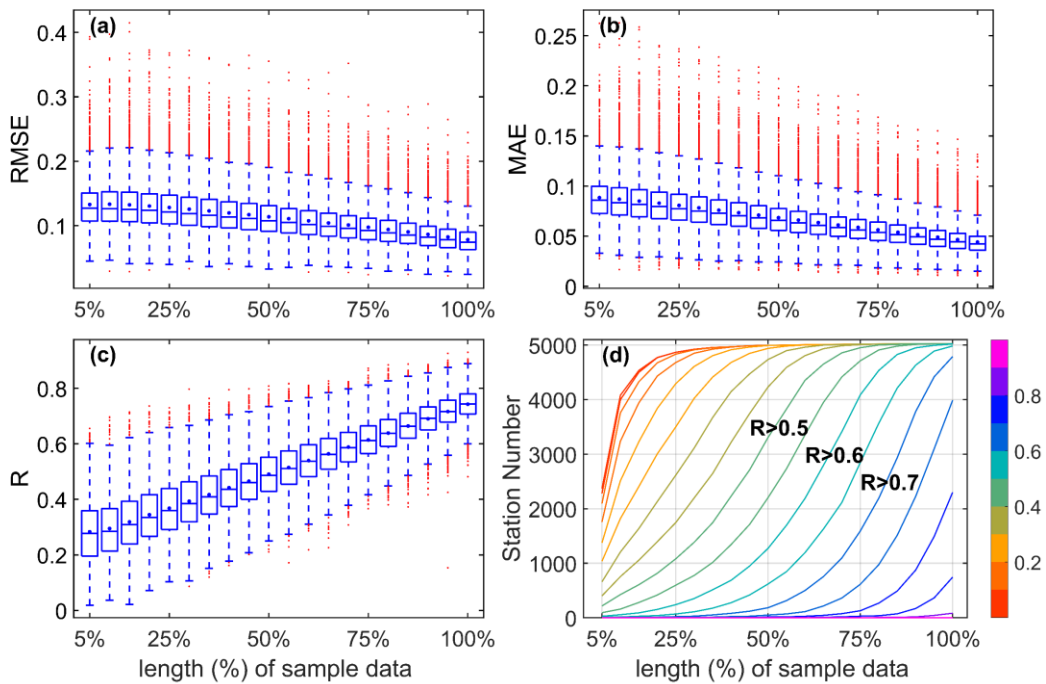
449 2.10 Workflow

450 Figure 2 summarizes the flowchart and provides an overview of the structure of this study, which
 451 involves four main parts: (1) data preprocessing, (2) model training, (3) validation and prediction,
 452 and (4) data gridding.

453 3 Results and discussion

454 3.1 Dependence of model performance on training data length

455



456

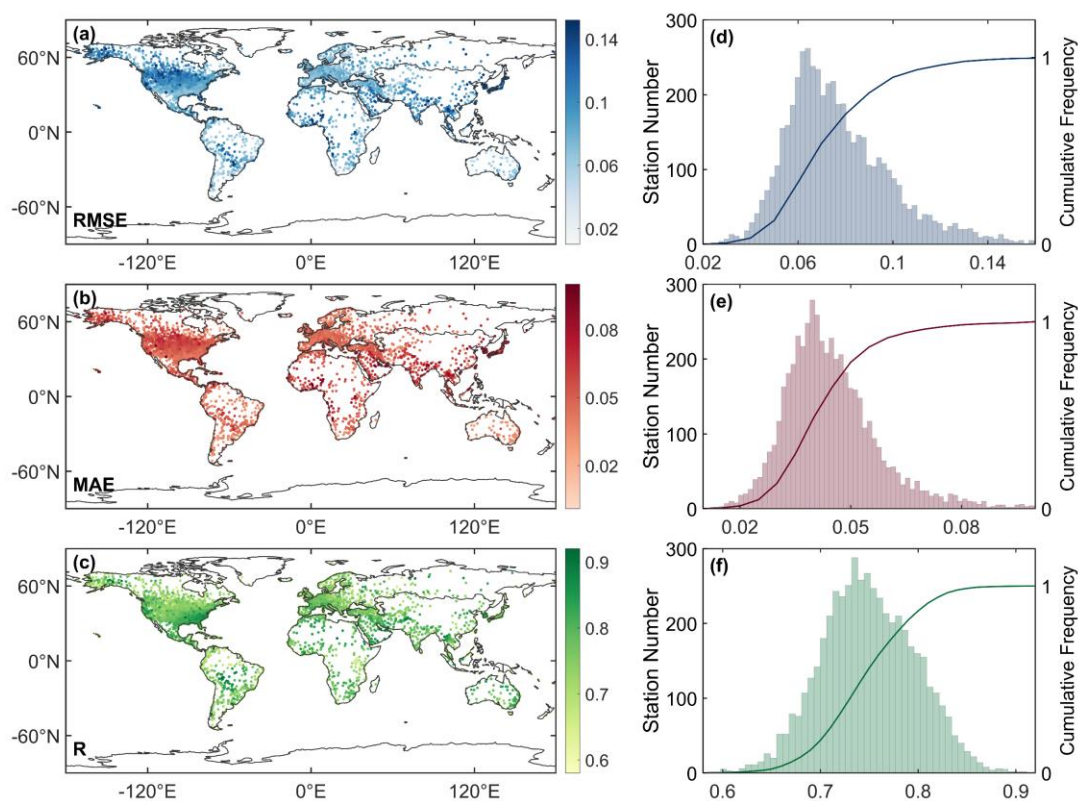
457 **Figure 3:** Boxplots of root mean squared error (RMSE) (a), mean absolute error (MAE) (b), and
 458 correlation coefficient (R) (c) between predicted values and target using different lengths of sample
 459 data (5% interval) as the training dataset, and the correlation coefficient curve (d) of the station
 460 number in the different lengths of sample data.

461 We build the models using different lengths of sample data (5% to 100%, with a 5% interval) by random
 462 allocation without overlap and evaluate the predictive performance of each model. Figure 3 depicts
 463 RMSE(a), MAE(b), and R (c) between the predicted values and target based on the training data of 5%
 464 to 100% sample data at a station. As the volume of the training data increases, the RMSE and MAE
 465 decrease, and the correlation coefficient increases. Compared to 5% of the sample data, the result of 100%
 466 sample data shows a decrease in RMSE by 41.1%, a decrease in MAE by 50.1%, and an increase in R
 467 by 162.3%. The relationship between the length of sample data and the model's performance is positive
 468 for each station. Figure 3 (d) shows that R of approximately 70% stations is greater than 0.5 at 50% of
 469 the sample data, while at 75%, the R of approximately 80% of stations is greater than 0.6. When 100%
 470 of the sample data is used as sample data, the R of approximately 80% of stations is greater than 0.75,
 471 and the R of about 97% is greater than 0.7. This finding indicates that the predictive capability and
 472 robustness of the model increase as the amount of training data increases. It may be attributed to the
 473 model's ability to capture more complex patterns and relationships among the input by multi-year data.

474 **3.2 Evaluation of model training**

475 Figure 4 shows the spatial distribution (a-c) and frequency and cumulative frequency (d-e) of RMSE,
 476 MAE, and R of all stations. The mean values of RMSE, MAE, and R are 0.078, 0.044, and 0.750,
 477 respectively. The RMSE of 93% stations is less than 0.11, the MAE of 91% is less than 0.06, and the R
 478 of 88% is greater than 0.7. The R values in Africa, Asia, Europe, North America, Oceania, and South
 479 America are 0.763, 0.758, 0.736, 0.750, 0.759, and 0.738, respectively. Although the RMSE and MAE
 480 of a few stations are high in America and Asia, the R is still high (>0.6). Therefore, the results of the

481 model's errors demonstrate that the model performs well on almost all stations.



482

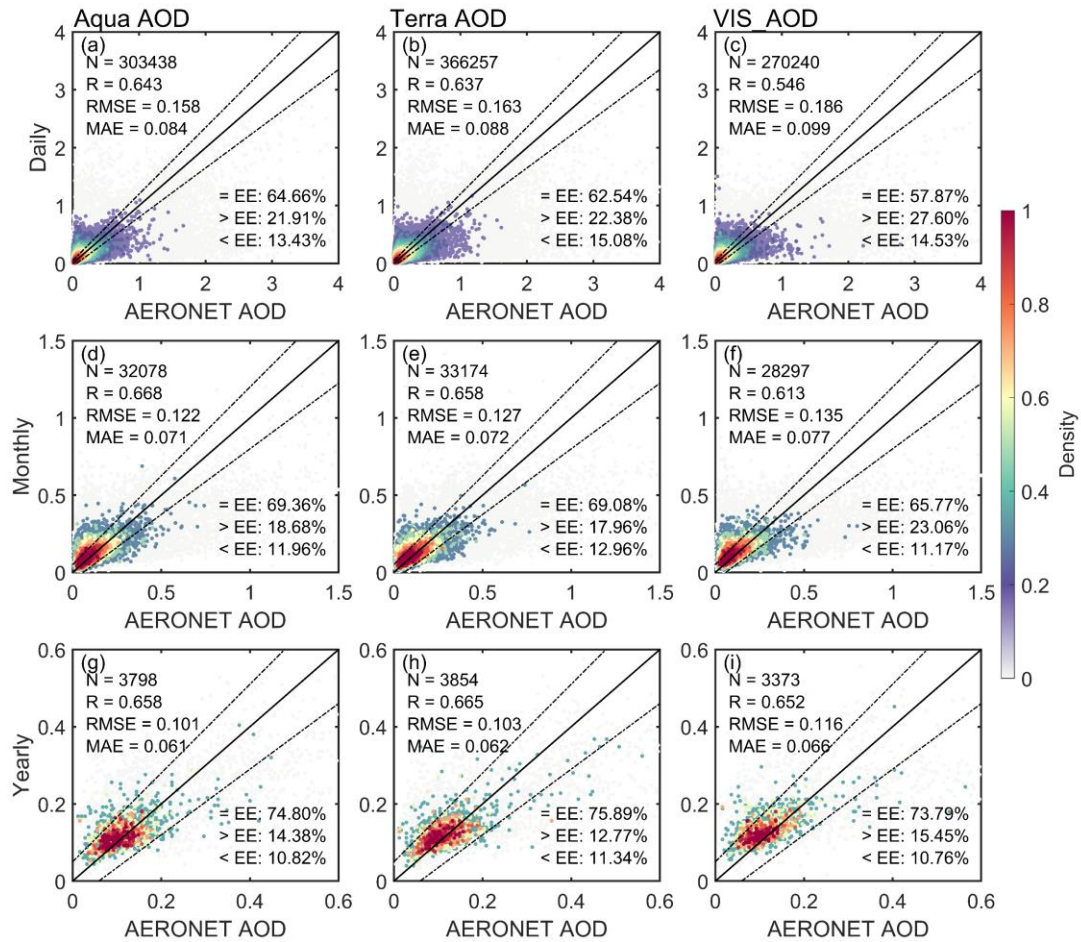
483 **Figure 4:** Spatial distribution (a-c) of root mean squared error (RMSE), mean absolute error (MAE),
484 and correlation coefficient(R) between the model's result and target with 100% sample data. Station
485 number (bar) and cumulative frequency (curve) (d-e) of RMSE, MAE, and R.

486 3.3 Validation and comparison with MODIS and AERONET AOD

487 3.3.1 Validation over global land

488 To validate the model's predictive ability, the visibility-derived AOD (for short, VIS_AOD) is compared
489 with Aqua, Terra and AERONET AOD at 550nm for the global scale. Among them, Aqua AOD has been
490 used as training data, which is not independent. Terra AOD and AERONET AOD have not been used as
491 training data and can be regarded as independent data.

492 First, the relationship among daily MODIS and AERONET AOD is evaluated. Figure 5 shows the scatter
493 density plots between AERONET AOD and Aqua AOD (a, d, g) and Terra AOD (b, e, h). The R values
494 with Aqua AOD and Terra AOD are 0.643 and 0.637 on the daily scale, and 0.668 and 0.658 on the
495 monthly scale, 0.658 and 0.665 on the yearly scale. The RMSE with Aqua AOD and Terra AOD are 0.158
496 and 0.163 on the daily scale, and 0.122 and 0.127 on the monthly scale, 0.101 and 0.103 on the yearly
497 scale. The MAE values with Aqua AOD and Terra AOD are 0.084 and 0.088 on the daily scale, and 0.071
498 and 0.072 on the monthly scale, 0.061 and 0.062 on the yearly scale. The percentages of sample point
499 falling within the EE envelopes are 64.66% and 62.54% on the daily scale, and 69.36% and 69.08% on
500 the monthly scale, 74.80% and 75.89% on the yearly scale.



501

502 **Figure 5:** Scatter density plots between AERONET AOD (550nm) and Aqua MODIS AOD, Terra
 503 MODIS AOD and VIS_AOD on the daily (a-c), monthly (d-f) and yearly (g-i) scale. The solid black line
 504 represents the 1:1 line and the dashed lines represents expected error (EE) envelopes. The sample size
 505 (N), correlation coefficient (R), mean absolute error (MAE), and root mean square error (RMSE) are
 506 given. ‘= EE’, ‘> EE’, and ‘< EE’ represent the percentages (%) of retrievals falling within, above, and
 507 below the EE, respectively. The matching time for Aqua AOD and VIS_AOD with AERONET AOD is
 508 13.30 (\pm 30 minutes) at local time, and the matching time between Terra AOD and AERONET AOD is
 509 10.30 (\pm 30 minutes) at local time.

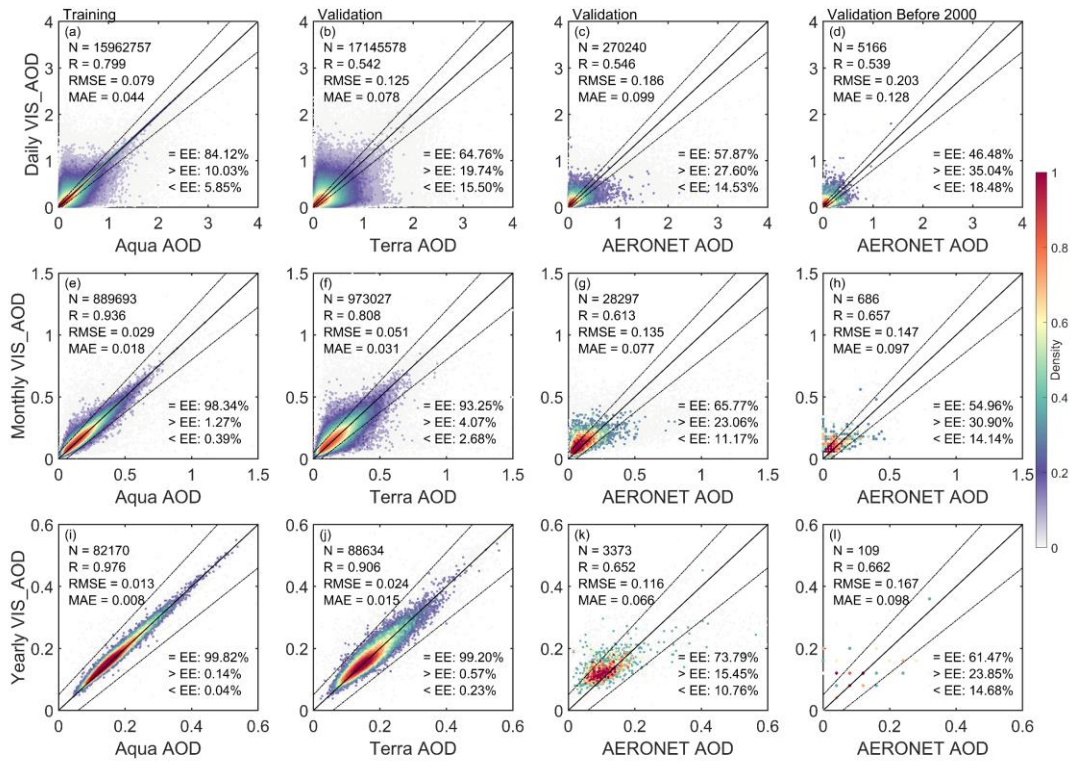
510 Figure 6 shows the scatter density plots and the EEs between VIS_AOD and Aqua AOD, Terra AOD,
 511 and AERONET AOD. Aqua AOD is not an independent validation, and Terra and AERONET AOD are
 512 independent validation. For the daily scale, the R, RMSE and MAE of between VIS_AOD and Aqua
 513 AOD (15,962,757 pairs data) is 0.799, 0.079 and 0.044, respectively. The percentage of sample point
 514 falling within the EE envelopes is 84.12% on the global scale (Figure 6 a). The R between VIS_AOD
 515 and Terra AOD (17,145,578 pairs data) is 0.542, with a RMSE of 0.125 and MAE of 0.078. The
 516 percentage falling within the EE envelopes is 64.76% (Figure 6 b). The R between VIS_AOD and
 517 AERONET AOD (270,240 pairs data) at 395 sites is 0.546, with a RMSE of 0.186 and MAE of 0.099.
 518 The percentage falling within the EE envelopes is 57.87% (Figure 6 c).

519 For the monthly and annual scales, RMSE and MAE show a significant decrease between VIS_AOD and
 520 Aqua, Terra, and AERONET AOD, and R and percentages falling within EE show a significant increase

521 in Figure 6 (e-g, i-k). The monthly RMSEs are 0.029, 0.051, and 0.135, the monthly MAEs are 0.018,
522 0.031, and 0.077, and the R values are 0.936, 0.808, and 0.613, respectively. The percentages falling
523 within the EE envelopes are 98.34%, 93.25%, and 65.77%. The RMSEs at the annual scale are 0.013,
524 0.024, and 0.116, the MAEs are 0.008, 0.015, and 0.066, and the R values are 0.976, 0.906, and 0.652,
525 respectively. The percentages falling within the EE envelopes are 99.82%, 99.20%, and 73.79%. The
526 percentage falling within the EE envelopes against AERONET is smaller than that against Terra, which
527 may be related to the elevation of AERONET sites, the distance between AERONET and meteorological
528 stations, and observed time. The results highlighted above demonstrate a clear improvement in
529 performance on the monthly and annual scales compared to the daily scale (Schutgens et al., 2017), which
530 provided a foundation for the gridded dataset.

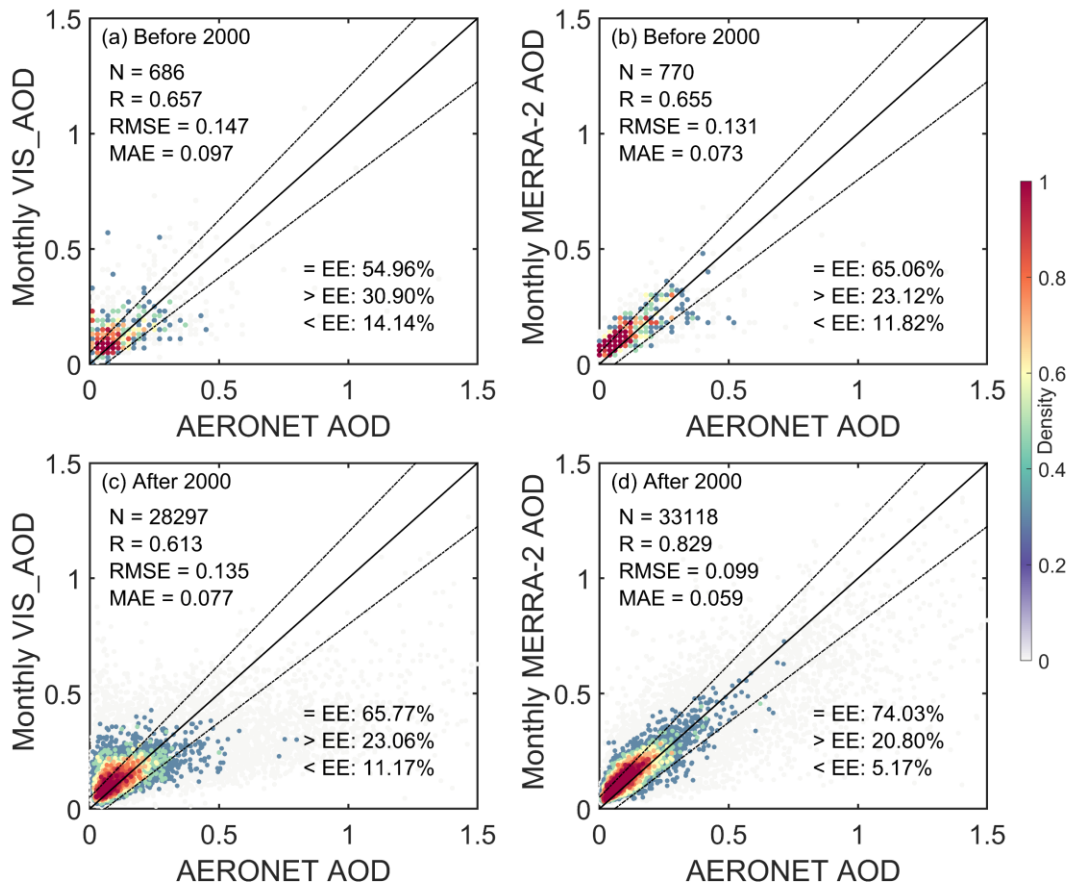
531 To further examine the predictive capability of historical data, we compare the VIS_AOD with
532 AERONET AOD before 2000, as shown in Figure 6 (d, h, l). We match 43 AERONET sites, with a total
533 of 5166 daily records. The result indicates that the daily-scale R is close to that after 2000 (Figure 6 c),
534 with the percentages approaching 50% falling within the EE envelopes. The monthly and annual
535 correlation coefficients are even higher, with a percentage of 55% falling within the EE envelopes.
536 Although the sample size is small, it still demonstrates the excellent predictive ability of the model.
537 Compared with AERONET (an independent validation dataset), the performance of VIS_AOD is almost
538 unchanged before and after 2000.

539 We also compare the VIS_AOD with the MERRA-2 reanalysis AOD on the monthly scales, as shown in
540 Figure 7. The correlation coefficient between MERRA-2 and AERONET is 0.655 before 2000, slightly
541 lower than the correlation coefficient (0.657) between VIS_AOD and AERONET. The correlation
542 coefficient between MERRA-2 and AERONET is 0.829 after 2000, significantly higher than that before
543 2000, while the correlation coefficient between VIS_AOD and AERONET is 0.613. It suggests that
544 VIS_AOD and MERRA-2 AOD have similar accuracy before 2000. The correlation of MERRA-2 after
545 2000 is higher and even performs better than MODIS retrievals (as shown in Figure 5) when evaluated
546 at AERONET sites. However, before 2000, the correlation coefficient of MERRA-2 and AERONET,
547 RMSE, and MAE all show significant changes and differences in consistency. The higher correlation
548 between MERRA-2 and AERONET AOD is partly because MERRA-2 has assimilated AERONET AOD
549 observations (Gelaro et al., 2017). Compared to AERONET, VIS_AOD and Aqua/Terra MODIS have a
550 similar correlation coefficient. The correlation coefficient of VIS_AOD before 2000 is even higher than
551 after 2000, and the changes in RMSE and MAE are not significant. It indicates good consistency of
552 VIS_AOD. In conclusion, the predicted results have good consistency with AERONET AOD and Terra
553 AOD on the daily scale. The monthly and annual results have a significant improvement. The model
554 shows good predictive capabilities before/after 2000, highlighting the stable accuracy of VIS_AOD.



555

556 **Figure 6:** Scatter density plots between predicted AOD (VIS_AOD) and Aqua MODIS AOD, Terra
 557 MODIS AOD, AERONET AOD and AERONET AOD before 2000 on the daily (a-d), monthly (e-h) and
 558 yearly (g-i) scale. The solid black line represents the 1:1 line and the dashed lines represents expected
 559 error (EE) envelopes. The sample size (N), correlation coefficient (R), mean absolute error (MAE), and
 560 root mean square error (RMSE) are given. ‘= EE’, ‘> EE’, and ‘< EE’ represent the percentages (%) of
 561 retrievals falling within, above, and below the EE, respectively. Note Aqua AOD is not an independent
 562 validation for predicted results, while Terra and AERONET are independent validation.



563

564 **Figure 7:** Scatter density plots between AERONET AOD and the predicted AOD (VIS_AOD) and
 565 MERRA-2 AOD before/after 2000 on the monthly scale. The solid black line represents the 1:1 line and
 566 the dashed lines represents expected error (EE) envelopes. The sample size (N), correlation coefficient
 567 (R), mean absolute error (MAE), and root mean square error (RMSE) are given. ‘= EE’, ‘> EE’, and ‘<
 568 EE’ represent the percentages (%) of retrievals falling within, above, and below the EE, respectively.

569 3.3.2 Validation over regions

570 Aerosol loading exhibits spatial variability. Evaluation metrics for the relationships between
 571 visibility-derived AOD and AERONET AOD and Terra AOD for each region are listed in Table 1.
 572 Over Europe and North America, the results are similar to those of Terra and AERONET, with a
 573 large number of data pairs, greater than 10^5 (AERONET) and greater than 10^7 except for Eastern
 574 Europe (Terra) on the daily scale. Approximately 63% -70% fall within the EE envelopes. The
 575 RMSE is approximately 0.1100, except for western North America, the MAE is approximately
 576 0.0700, with a correlation coefficient between 0.44 and 0.54.

577 Over Central South America, South Africa, and Australia, data pairs are about 10^{3-4} (AERONET)
 578 and 10^6 (Terra) on the daily scale. 52-60% fall within the EE envelopes compared to AERONET,
 579 and 58-67% compared to Terra. The RMSE is 0.03-0.05 compared to Terra, and 0.11-0.17 compared
 580 to AERONET. The correlation coefficient ranges from 0.4 to 0.74, with the highest correlation
 581 coefficient in South America at 0.740.

582 In Asia, India, and West Africa, the data pairs are only approximately 10^4 (AERONET). 32% to 50%

583 fall within the EE envelopes compared to AERONET, the RMSE ranges from 0.2 to 0.5, and the
584 MAE ranges from 0.11 to 0.36. 51 to 58%, compared to Terra, fall within the EE envelopes, the
585 RMSE is around 0.16, and the MAE is around 0.11. Compared to AERONET, in these high aerosol
586 loading regions, RMSE and MAE increase, and the percentages falling within the EE envelopes
587 decrease, but the correlation coefficients do not significantly decrease.

588 Compared to Terra AOD, 55% -67% of data falls within the EE envelopes on the daily scale, 87% -
589 96% on the monthly scale, and over 97% on the yearly scale. Compared to AERONET AOD, 32-
590 68% of data falls within the EE envelopes, 24% -84% on the monthly scale, and 15% -97% on the
591 yearly scale. On both monthly and yearly scales, all metrics have shown a significant increase in
592 performance when compared to Terra. However, compared to AERONET, not all metrics increase
593 in some regions due to limited data pairs, such as West Africa, Northeast Asia, and India, which may
594 be due to the spatial differences between AERONET sites and meteorological stations.

595 **3.3.3 Validation at a site scale**

596 Sites, especially AERONET, are not completely uniform across the world or in any region, and
597 different stations have different sample sizes, which may lead to a certain uncertainty. Therefore,
598 further analysis was conducted on the spatial distribution of different evaluation metrics. Figure 8
599 shows the validation and comparison of daily VIS_AOD against Terra and AERONET AOD at a
600 site scale.

601 Compared to Terra daily AOD, the R of 67% stations is greater than 0.4, the mean bias of 83% is

Table 1: Evaluation metrics for the relationships between visibility-derived AOD and AERONET AOD and Terra AOD for each region.

Region		N			R			RMSE			MAE			Within EE (%)		
		daily	monthly	yearly	daily	monthly	yearly	daily	monthly	yearly	daily	monthly	yearly	daily	monthly	yearly
Eastern Europe	AERONET	21724	2317	271	0.463	0.493	0.653	0.1069	0.0647	0.0326	0.0714	0.0442	0.0263	65.69	83.77	97.42
	TERRA	661630	36435	3278	0.464	0.665	0.790	0.1095	0.0471	0.0214	0.0726	0.0286	0.0122	66.07	94.71	99.18
Western Europe	AERONET	53043	6033	697	0.445	0.487	0.344	0.1089	0.0716	0.0513	0.0711	0.0474	0.0347	64.40	79.21	89.10
	TERRA	1778013	104620	9166	0.467	0.763	0.811	0.1096	0.0391	0.0210	0.0712	0.0268	0.0124	66.99	95.42	99.40
Western North America	AERONET	33859	2948	334	0.503	0.484	0.509	0.1465	0.0949	0.0566	0.0747	0.0597	0.0419	63.58	67.37	81.14
	TERRA	1725226	82734	7201	0.542	0.765	0.906	0.1144	0.0465	0.0180	0.0671	0.0267	0.0125	69.48	94.42	99.61
Eastern North America	AERONET	47407	5359	608	0.527	0.526	0.559	0.1135	0.0824	0.0436	0.0657	0.0472	0.0331	67.52	77.78	87.50
	TERRA	6280277	359520	31343	0.515	0.799	0.847	0.1159	0.0435	0.0165	0.0726	0.0275	0.0111	66.70	94.94	99.80
Central South America	AERONET	10911	1176	149	0.740	0.811	0.866	0.1735	0.1272	0.1060	0.1021	0.0904	0.0688	52.40	47.96	67.79
	TERRA	444780	26362	2410	0.545	0.820	0.776	0.1447	0.0591	0.0369	0.0909	0.0396	0.0219	58.48	89.29	97.39
Southern Africa	AERONET	4255	309	38	0.423	0.480	0.630	0.1553	0.1128	0.0705	0.1033	0.0805	0.0525	52.08	59.55	78.95
	TERRA	216239	11304	1118	0.518	0.821	0.870	0.1258	0.0511	0.0296	0.0836	0.0340	0.0191	60.64	91.70	98.21
Australia	AERONET	6426	516	63	0.488	0.654	0.363	0.1094	0.0827	0.0725	0.0711	0.0620	0.0563	59.96	59.88	71.43
	TERRA	284693	14588	1286	0.398	0.784	0.831	0.1091	0.0363	0.0188	0.0666	0.0261	0.0143	67.01	94.65	99.38
Western Africa	AERONET	2205	205	34	0.553	0.594	0.762	0.3180	0.2873	0.3357	0.2082	0.2029	0.2587	37.96	40.00	23.53
	TERRA	156392	10468	1028	0.501	0.769	0.849	0.1769	0.0706	0.0412	0.1198	0.0482	0.0242	51.83	88.01	97.57
Southeast Asia	AERONET	4134	504	74	0.405	0.542	0.488	0.2037	0.1447	0.1198	0.1274	0.0988	0.0821	50.17	56.15	60.81
	TERRA	402465	27058	2500	0.470	0.753	0.872	0.1730	0.0729	0.0342	0.109	0.0455	0.0198	57.25	87.01	97.96
Eastern China	AERONET	7396	927	118	0.513	0.551	0.356	0.3571	0.2355	0.1933	0.2038	0.1392	0.1382	40.10	49.84	50.00
	TERRA	241185	17324	1518	0.523	0.811	0.895	0.1646	0.0638	0.0302	0.1073	0.0435	0.0225	55.77	88.07	98.88
Northeast Asia	AERONET	9979	1178	142	0.569	0.593	0.367	0.4941	0.3249	0.2604	0.2924	0.2425	0.2202	35.17	29.54	21.13
	TERRA	78823	5485	467	0.553	0.872	0.965	0.1973	0.0636	0.0263	0.1201	0.0440	0.0198	56.48	87.77	98.29

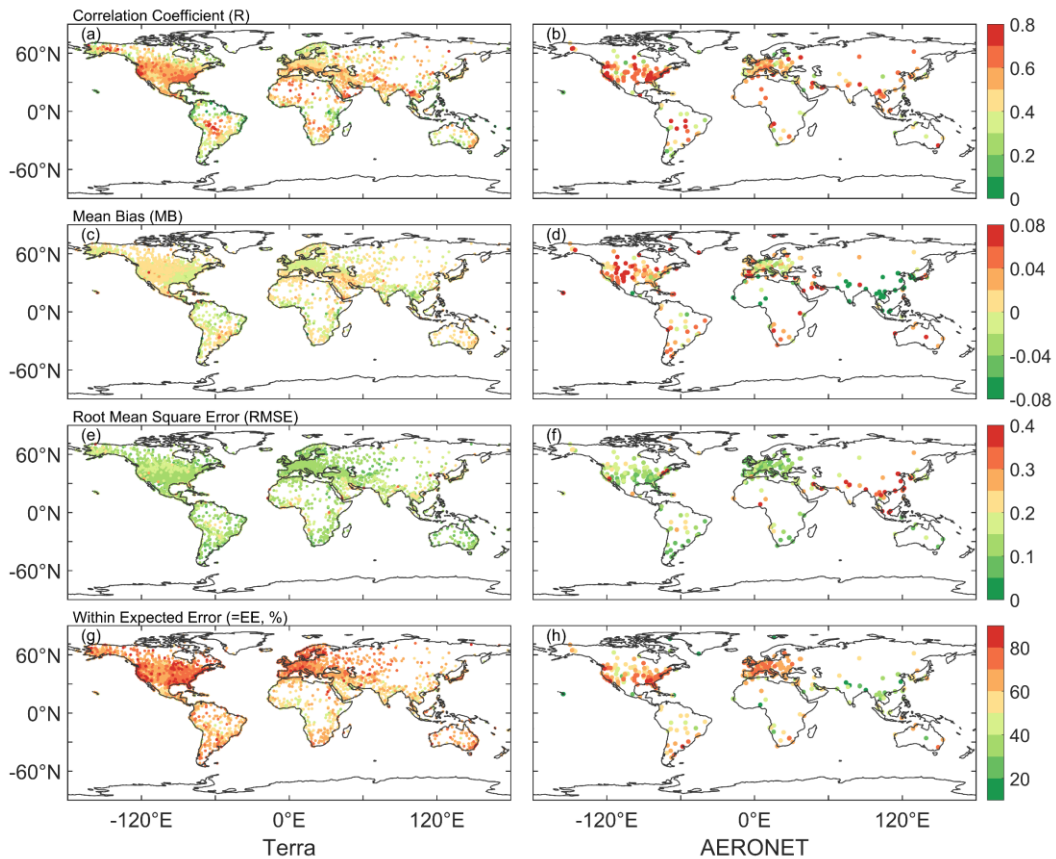
<i>India</i>	<i>AERONET</i>	2208	203	32	0.521	0.462	0.534	0.2957	0.3015	0.3588	0.2049	0.2283	0.2862	32.11	24.63	15.63
	<i>TERRA</i>	179928	9564	862	0.526	0.815	0.915	0.1564	0.0599	0.0352	0.1089	0.042	0.0238	55.16	90.43	98.14

603

604 less than 0.01, the RMSE of 85% is less than 0.15, and the percentage falling within the EE of 67%
605 is greater than 60%. More than 85% of stations fall within the EE is greater than 60% in Europe,
606 North America, and Oceania, while 40-60% in South America, Africa, and Asia. The percentage of
607 expected error is low in South and East Asia, and Central Africa, with some underestimation. Above
608 60% in Africa, Asia, North America, and Europe have a correlation coefficient greater than 0.4. The
609 regions with lower correlation are the coastal regions of South America, eastern Africa, western
610 Australia, northeastern North America, and northern Europe. Above 90% of the RMSE in Europe,
611 North America, and Oceania have a correlation coefficient smaller than 0.15. High RMSE regions
612 are in western North America, Asia, central South America, and central Africa.

613 Compared to AERONET daily AOD, the R of 74% stations is greater than 0.4, and the spatial
614 distribution is similar to Terra's. The mean bias of 44% is less than 0.01, the RMSE of 68% is less
615 than 0.15, and the percentage falling within the EE of 53% is greater than 60%. More than 70% of
616 sites have a correlation coefficient greater than 0.4 in Africa, Asia, Europe, and North America.
617 More than 57% of sites have an expected error percentage of over 60% in Europe, North America,
618 and Oceania, except for Asia. Over 72% of sites have a RMSE less than 0.15. Except for Oceania
619 and South America, over 71% of sites in other regions have MAE less than 0.01. Almost all sites in
620 Asia show a negative bias, significantly underestimating. However, there is a significant
621 overestimation in western North America and western Australia. Most sites in Asia falling within
622 the expected error are less than 50%. High RMSE are in high emission and dust areas, such as Asia,
623 India, and Africa.

624 The validation and comparison on the site scale show a limitation similar to the MODIS DT
625 algorithm. In areas with high vegetation coverage, the AOD from visibility are better than those in
626 bright areas. Although the correlation coefficients are high in high aerosol loading areas (Central
627 South America, West Africa, India, Eastern China, Northeast Asia), there are significant differences
628 in these areas with high RMSE values. As shown in Figure 6, some stations located in dusty and
629 urban areas are overestimated or underestimated. Studies have shown that there is significant
630 uncertainty in the MODIS retrievals in these regions, and the challenges of inversion algorithms are
631 significant in bright surfaces (desert and snow covered areas) and urban surface of densely
632 populated complex structures (Chu et al., 2002; Remer et al., 2005; Levy et al., 2010; Wei et al.,
633 2019; Wei et al., 2020). In India, the elevation difference between AERONET site and
634 meteorological station reached 0.7km may be a factor affecting the validation effect, as aerosol
635 varies greatly with altitude. In eastern China, the complex urban surface, emission sources, and
636 observations in different locations (AERONET site and meteorological station) may be the reasons
637 for underestimation. At the same time, visibility stations in desert areas are sparse, and the spatial
638 variability of dust aerosols is large, which also increases the difficulty to estimate VIS_AOD.



639
 640 **Figure 8:** Validation of VIS_AOD against Terra and AERONET AODs at each site: (a–b)
 641 correlation (R), (c–d) mean bias (MB), (e–f) root mean square error (RMSE), (g–h) percentage (%)
 642 of VIS_AOD within the expected error envelopes.

643 3.3.4 Discussion and uncertainty analysis

644 The atmospheric visibility is a horizontal physical quantity, while AOD is a column-integrated
 645 physical quantity. We have linked the two variables together using machine a learning method,
 646 which partially compensates for the scarcity of AOD data. However, we have to face some
 647 limitations. Although the boundary layer height is considered, it is not sufficient. Pollutants such as
 648 smoke from biomass burning, dust, volcanic ash, and gas-aerosol conversion of sulfur dioxide to
 649 sulfate aerosols in the upper and lower troposphere can undergo long-range aerosol transport under
 650 the influence of circulation. The pollution transport and aerosol conversion processes above the
 651 boundary layer are still significant and cannot be ignored (Eck et al., 2023). Compared to surface
 652 visibility, bias occurs when the aerosol layer rises and affects AERONET measurements and
 653 MODIS retrievals. Therefore, it should be considered when using this data. If there were sufficient
 654 historical vertical aerosol measurements with high temporal and spatial resolution, the results of this
 655 data would be greatly improved. Although some studies use aerosol profiles from pollution transport
 656 models or assumed profiles as substitutes for observed profiles (Li et al., 2020; Zhang et al., 2020),
 657 the biases introduced by these non-observed profiles are still significant.

658 In machine learning, we use MODIS Aqua AOD as the target value for the model because the
 659 validation results for MODIS C6.1 product have a correlation coefficient of 0.9 or higher with
 660 AERONET AOD on the daily scale (Wei et al., 2019; Wei et al., 2020). Compared to AERONET,
 661 MODIS AOD provides more sample data with a high global coverage. However, apart from

662 modeling errors, the systematic biases and uncertainties of MODIS Aqua AOD cannot be ignored
663 (Levy et al., 2013; Levy et al., 2018; Wei et al., 2019). Averaging over time scale can reduce
664 representation errors effectively, and emission sources and orography can increase representation
665 errors (Schutgens et al., 2017). Therefore, the strong correlation at monthly and annual scales
666 indicates a substantial reduction in errors. This is also one of the reasons why this dataset shows
667 stronger correlation with Terra AOD and weaker correlation with AERONET in validation.

668 The spatial matching between meteorological stations and AERONET sites may cause some biases.
669 AERONET sites are usually not co-located with meteorological stations in terms of elevation and
670 horizontal distance, this is another reason for the weak correlation between VIS_AOD and
671 AERONET AOD. The meteorological stations are located at the airport. Different horizontal
672 distances may result in meteorological stations and AERONET sites being located on different
673 surfaces (such as urban, forest, mountainous). Differences in site elevation significantly impact the
674 relationship between AOD and measured visibility. When the AERONET site is at a higher elevation
675 than the meteorological station, there may be fewer measurements of aerosols over the sea at the
676 AERONET site.

677 Different pollution levels and station elevation affect the AOD derived from visibility. The elevation
678 difference and distance between meteorological stations and AERONET sites also have an impact
679 on the validation results. Therefore, the error and performance of different AERONET AOD values,
680 station elevation, and distance are analyzed.

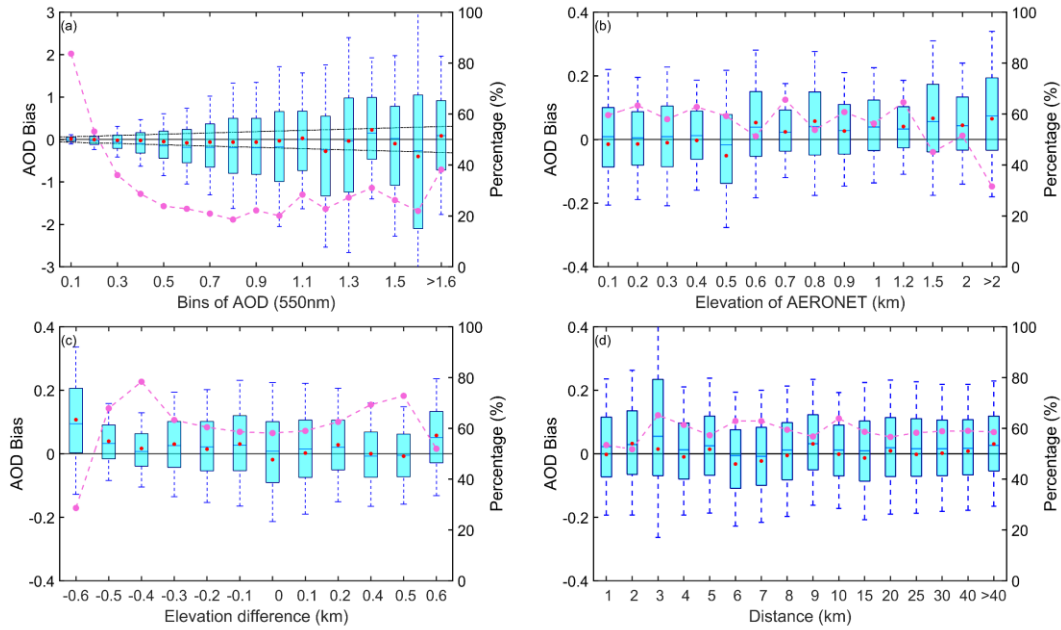
681 As the AOD increases, the variability of bias also increases in Figure 9 (a). Almost all mean bias
682 values are within the envelope of EE, except for 1.1-1.2 and 1.5-1.6. The average bias is 0.015
683 (AOD < 0.1), with 83% of data within the EE envelopes. The mean bias is -0.0011 (AOD, 0.1-0.2),
684 with 54% within the EE envelopes. The mean bias is negative (AOD, 0.3-1.0), with 20%-40%
685 falling within the EE envelopes. There is a positive bias (AOD, 1.1, 1.4 and >1.6), and there is a
686 negative bias at 1.2-1.3 and 1.5-1.6. The results indicate that as pollution level increases, the
687 negative mean bias becomes significant and the underestimation increases.

688 The contribution of particulate matter near the ground to the column aerosol loading is significant.
689 The elevation of the site affects the measurement of column aerosol loading in Figure 9 (b). There
690 is a negative bias in the low elevation (≤ 0.5 km) with a percentage of 60%-64% falling within the
691 EE envelopes and a positive bias in high elevation (0.5-1.2km) with a percentage of 50%-65%
692 falling within the EE envelopes. The percentage significantly decreases (> 1.2 km), and the average
693 bias increases. Therefore, the elevation of AERONET's site will cause bias in validation, and the
694 uncertainty greatly increases in high elevation.

695 Due to the elevation difference between the meteorological station and AERONET site in the
696 vertical direction, the uncertainty caused by elevation differences of site was analyzed in Figure 9
697 (c). When the elevation difference is negative (the elevation of the meteorological station is lower
698 than that of the AERONET station), there is a significant positive bias. When the difference is
699 positive, the mean bias approaches 0 or is positive. The percentage is greater than 60% (-0.5 km-
700 0.5km). The positive mean bias is greater than the negative mean bias, and the uncertainty greatly
701 increases when the elevation of meteorological stations is lower than that of AERONET sites. It
702 indicates that the contribution of the near surface aerosol to the column aerosol loading is significant
703 and cannot be ignored.

704 The spatial variability of aerosols is significant. Meteorological stations and AERONET sites are
705 not collocated, resulting in a certain distance in spatial matching. In this study, the upper limit of

706 distance is 0.5 degree. Figure 9 (d) shows the error of the distance between stations, where the
 707 degree is converted to the distance at WGS84 coordinates. The bias does not change significantly
 708 with increasing distance. The average bias is around 0, with the maximum positive mean bias
 709 (0.0322) at a distance of 2km and the maximum negative mean deviation (-0.0323) at 6km. The
 710 median is almost positive, except at 5km and 6km. The percentage falling within the EE envelopes
 711 is over 50%, with the maximum percentage (66%) at 3km and the minimum (62%) at 2km.



712

713 **Figure 9:** Box plots of AOD bias and the percentage falling within the EE envelopes (curves): (a)
 714 AERONET AOD levels, (b) elevation of AERONET sites, (c) elevation difference between
 715 meteorological stations and AERONET sites, (d) distance (km) between meteorological stations and
 716 AERONET sites. The black horizontal line represents the zero bias. For each box, the upper, lower,
 717 and middle horizontal lines, and whiskers represent the AOD bias 75th and 25th percentiles, median,
 718 and 1.5 times the interquartile difference, respectively. The black solid lines represent the EE
 719 envelopes ($\pm(0.05+0.15 \cdot \text{AOD}_{\text{AERONET}})$). No site with a difference of +0.3km (x-axis label without
 720 0.3) in (c).

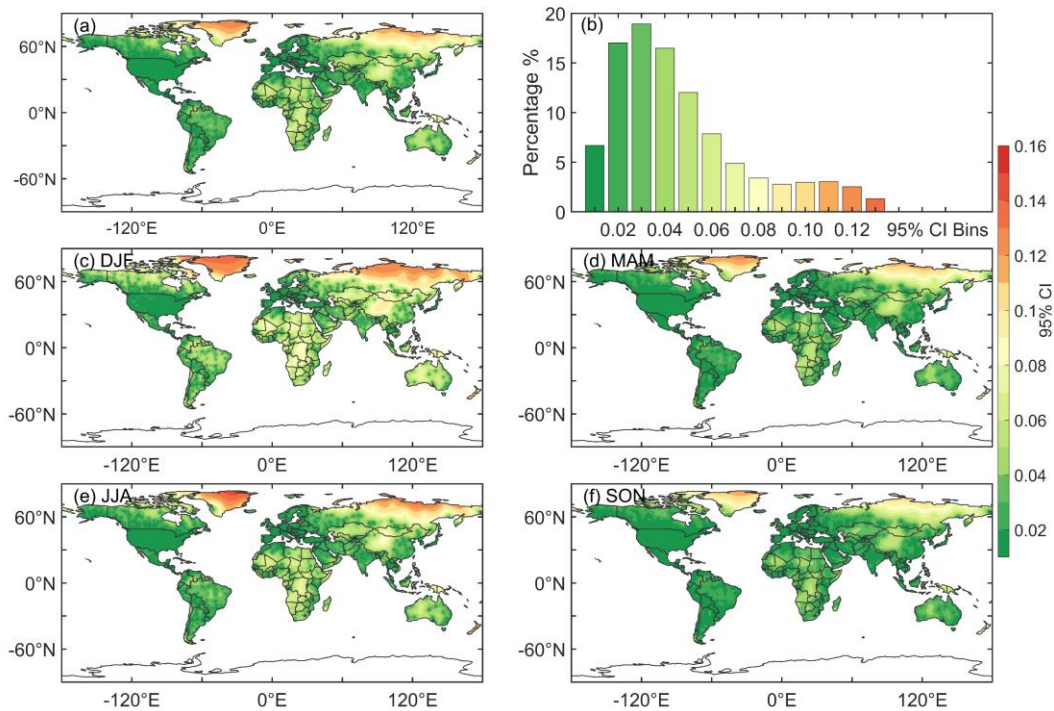
721 3.4 Gridded visibility-derived AOD

722 3.4.1 Uncertainty of gridded AOD

723 We calculate the width of the 95% CI for gridded AOD. Figure 10 (a-b) shows the spatial distribution
 724 and frequency of the 95% CI from 1980 to 2021. In areas with dense visibility stations, the kriging
 725 variance is low, the width of 95% CI is small, and the uncertainty of the gridded AOD is low. In
 726 areas with sparse visibility stations, the width is large, and the uncertainty is high. The uncertainty
 727 of approximately 43% of the grids is less than 0.03, and nearly 80% has an uncertainty less than
 728 0.06. Approximately 7% of the grids have an uncertainty larger than 0.1. Regions with low
 729 uncertainty are mainly located in North America (<60°N), Europe, Western and Southern Asia,
 730 Eastern China, and South America. Regions with high uncertainty are found in high-latitude areas
 731 (e.g., Siberia), high-altitude regions (e.g., Tibetan Plateau), and desert areas (such as the Sahara

732 Desert, Taklamakan Desert, and Australian deserts).

733 Uncertainty also exhibits seasonal variations, as shown in Figures (c-f). The percentage of grid cells
734 with uncertainty less than 0.06 is 63%, 84%, 77%, and 86% in DJF, MAM, JJA, and SON,
735 respectively. Compared to other seasons, uncertainty increases significantly in high-latitude regions,
736 Africa, northern Asia, Oceania, and eastern South America during DJF. In JJA, the distribution of
737 uncertainty is similar to DJF, but the uncertainty decreases. In MAM and JJA, there is higher
738 confidence, with a small number of grid cells having large uncertainty (>0.1), primarily concentrated
739 in high-latitude regions.



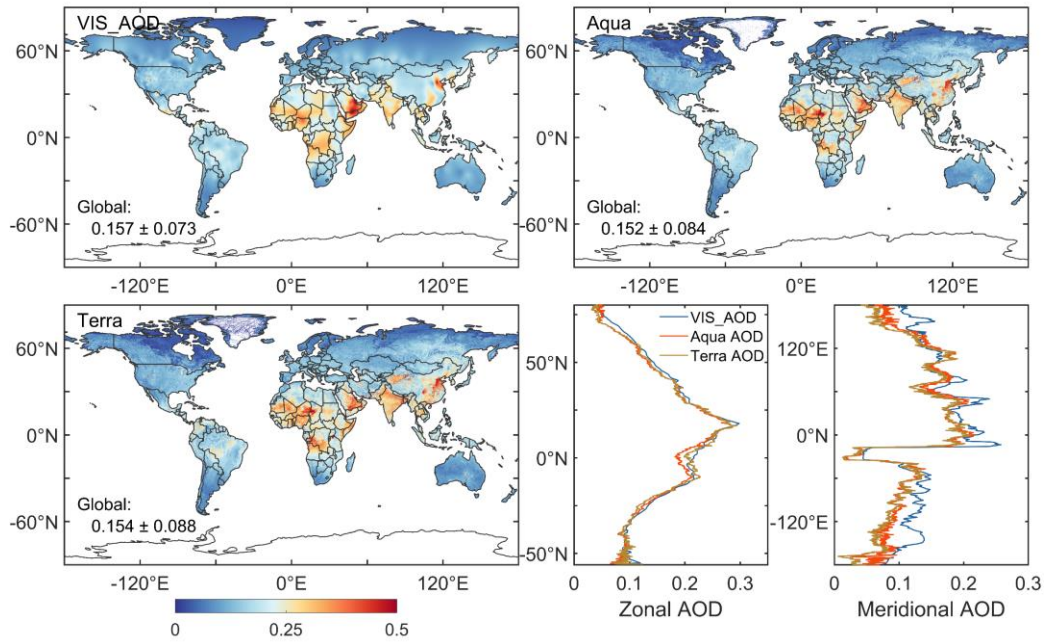
740

741 **Figure 10:** The spatial distribution (a) and frequency (b) of the 95% confidence interval (CI) from
742 1980 to 2021. The spatial distribution of the width of the 95% CI for each season (c-f). Bins of 95%
743 CI are from 0 to 0.15 with an interval of 0.01. DJF represents December and next January and
744 February. MAM represents March, April, and May. JJA represents June, July, and August. SON
745 represents September, October, and November.

746 3.4.2 Comparison with Aqua/Terra MODIS AOD

747 Figure 11 shows the gridded AOD based on ordinary kriging interpolation with the area-weighted
748 method and compares the multi-year spatial, zonal, and meridional distributions of AOD with Aqua
749 and Terra AOD over land from 2003 to 2021. The VIS_AOD is 0.157 ± 0.073 over land, which is
750 almost equal to the Aqua (0.152 ± 0.084) and Terra (0.154 ± 0.088) AOD values with relative biases
751 of 3.3%, and 1.9%, respectively. In order to compare the spatial correlation, Aqua and Terra MODIS
752 AOD are averaged to the 0.5-degree resolution. In the heatmap (Figure 12), the R of VIS_AOD and
753 Aqua AOD is 0.798, the RMSE is 0.049 with a bias of 32% compared to the mean, and the MAE is
754 0.008, with a bias of 5% compared to the mean. Compared to Terra AOD, the R is 0.787, and the
755 RMSE is 0.051, with a bias of 33% compared to the mean, and the MAE is 0.005, with a bias of 3%
756 compared to the mean. The R between Aqua and Terra AOD is 0.980. The R values between

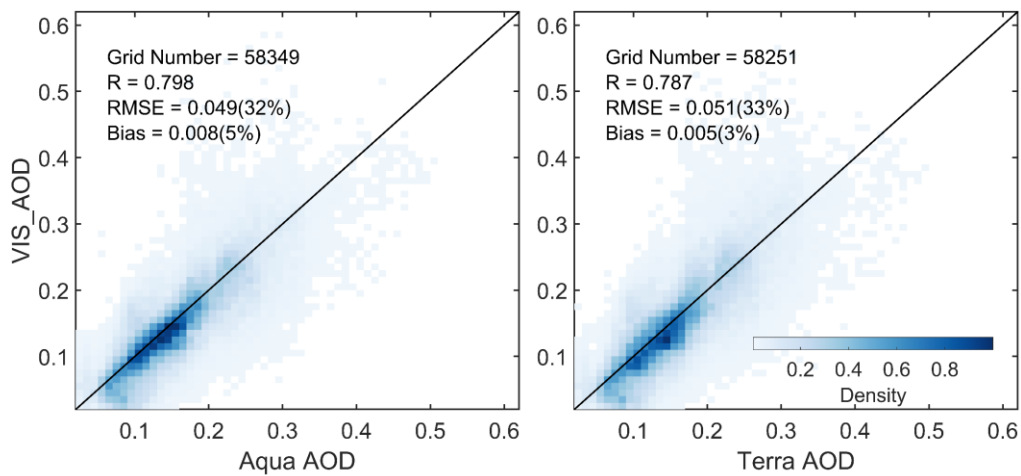
757 VIS_AOD and Aqua and Terra AOD are 0.995 and 0.990 for the zonal distribution and 0.986 and
 758 0.897 for the meridional distribution, respectively. In the low aerosol loading region, VIS_AOD
 759 exhibits a little overestimation. Whether in meridional or zonal distribution, the peak and valley
 760 regions are basically consistent (Tian et al., 2023). Due to the limitations of satellite inversion
 761 algorithms, a bias appears on the bright surface, especially in northern North America with extensive
 762 snow cover (Levy et al., 2013). All above results suggest that the gridded AOD is consistent with
 763 satellite retrievals in spatial distribution.
 764



765

766 **Figure 11:** The spatial, zonal and meridional distributions of the multi-year mean VIS_AOD, Aqua
 767 AOD, and Terra AOD over land from 2003 to 2021.

768



769

770 **Figure 12:** Heatmap of multi-year mean gridded VIS_AOD and Aqua AOD and Terra AOD during
 771 2003-2021. Terra and Aqua AOD are averaged onto a grid of 0. 5°.

772 3.5 Interannual variability and trend of visibility-derived AOD over global land

773 The spatial distribution of multi-year average AOD from 1980 to 2021 over land is shown in Figure
774 13 (a). The mean AOD of land (-60-85°N), Northern Hemisphere (NH, 0-85°N), and the Southern
775 Hemispheres (SH, -60-0°N) is 0.161 ± 0.074 , 0.158 ± 0.076 , and 0.173 ± 0.059 , respectively. The
776 AOD values of Africa, Asia, Europe, North America, Oceania, and South America are 0.241, 0.222,
777 0.110, 0.111, 0.129 and 0.117, respectively.

778 Due to the influence of geography, atmospheric circulation, population, and emissions, the AOD
779 varies in different latitudes. Figure 14 illustrates the multi-year average AOD in different latitude
780 ranges for land, the NH, and the SH from 1980 to 2021. Within [-20, 20°N], the global average AOD
781 reaches its maximum (0.234), and the maximum AOD NH is 0.256 in [0, 20°N]. The highest AOD
782 in SH is 0.217 in [-15, 0°N]. The average AOD in SH rapidly decreases from -15°N to -35°N. In
783 NH, AOD is generally greater than in SH from 5°N to 65°N. When, the latitude is greater than 70°N,
784 the NH's AOD is smaller than the SH's.

785 There are many regions of high AOD values occur in NH, with the distribution of population density.
786 Approximately 7/8 of the global population resides in the NH, with 50% concentrated at 20°N-40°N
787 (Kummu et al., 2016), indicating a significant impact of human activities on aerosols. The highest
788 AOD values are observed near 17°N, including the Sahara Desert, Arabian Peninsula, and
789 southeastern India, suggesting that in addition to anthropogenic sources, deserts also play a crucial
790 role in aerosol emissions. Lower AOD regions of the SH are from 25°S to 60°S, encompassing
791 Australia, southern Africa, and southern South America, indicating lower aerosol burdens in these
792 areas. Additionally, North America also exhibits low aerosol loading. Chin et al. (2014) analyzed
793 the AOD over land from 1980 to 2009 with the Goddard Chemistry Aerosol Radiation and Transport
794 model, which is similar to the visibility-derived AOD. The spatial distribution is consistent with the
795 satellite results (Remer et al., 2008; Hsu et al., 2012; Hsu et al., 2017; Tian et al., 2023). The AOD
796 and extinction coefficient retrieved from visibility show a similar distribution at global scale, with
797 a correlation coefficient of nearly 0.6 (Mahowald et al., 2007). Similar global (Husar et al., 2000;
798 Wang et al., 2009) and regional (Koelemeijer et al., 2006; Wu et al., 2014; Boers et al., 2015; Zhang
799 et al., 2017; Zhang et al., 2020) spatial distributions have been reported.

800 AOD loadings exhibit significant seasonal variations worldwide, particularly over land. In this study,
801 a year is divided into four parts: December-January-February (DJF), March-April-May (MAM),
802 June-July-August (JJA), and September-October-November (SON), corresponding to winter
803 (summer), spring (autumn), summer (winter), and autumn (spring) in NH (SH), respectively. Figure
804 13 (b-e) also depicts the spatial distribution of seasonal average AOD over land from 1980 to 2021.
805 The global AOD in DJF, MAM, JJA, and SON is 0.158 ± 0.062 , 0.162 ± 0.081 , 0.175 ± 0.093 , and
806 0.153 ± 0.070 , respectively. The standard bias of AOD in JJA and MAM are greater than those in
807 DJF and SON. AOD exhibits seasonal changes, with the highest in JJA, followed by MAM, DJF,
808 and SON. From 1980 to 2021, the seasonal AOD in NH is 0.152 ± 0.064 (DJF), 0.161 ± 0.088 (MAM),
809 0.176 ± 0.090 (JJA), and 0.144 ± 0.060 (SON), and in SH is 0.184 ± 0.041 (DJF), 0.166 ± 0.044 (MAM),
810 0.169 ± 0.072 (JJA), and 0.19 ± 0.060 (SON).

811 In NH, the AOD ranking from high to low in season is summer > spring > winter > autumn. In SH,
812 the AOD ranking from high to low in season is spring > summer > winter > autumn. The highest
813 AOD is observed during JJA in NH, while in SH, the peak occurs during SON. The occurrence of

814 high AOD values is highly associated with the growth of hygroscopic particle and the photochemical
815 reaction of aerosol precursors under higher relative humidity in Asia (JJA) (Remer et al., 2008) and
816 Europe such as Russia (JJA), and biomass burning in South America (SON), Southern Africa (SON),
817 and Indonesia (SON) (Ivanova et al., 2010; Krylov et al., 2014). On the other hand, the lowest global
818 AOD values are observed during autumn, which may be attributed to the weakening of monsoon
819 systems (Li et al., 2016; Zhao et al., 2019).

820 In addition to the spatial characteristics of AOD, the temporal variations in AOD have also been of
821 great interest due to the significant relationship between aerosols and climate change. Figure 13 (f)
822 shows the temporal trends of annual average AOD (** represents passing the significance test,
823 $p < 0.01$) over the global land, the SH and the NH during 1980-2021. The global land, NH, and SH
824 trends demonstrate decreasing trends of AOD with values of $-0.0026/10a$, $-0.0018/10a$, and $-$
825 $0.0059/10a$, respectively, with all passing the significance test with a confidence level of 95%.
826 Notably, the declining trend is much greater in the SH than in the NH. It may be related to the
827 decrease in the frequency of sandstorms and wildfires and the increase in precipitation, such as in
828 Australia. Two AOD peaks in 1983 and 1994 and two AOD valleys in 1980 and 1990 are observed
829 before 2000. The two AOD peaks may be attributed to large volcanic eruptions, which has been
830 confirmed by previous studies. The volcanic eruptions and their associated fires of the El Chichón
831 volcano in Mexico in 1982 (Hirono and Shibata, 1983) and Mount Pinatubo in the Philippines in
832 1991 (Tupper et al., 2005) resulted in elevating global AOD levels in the following years. The AOD
833 recovery to the previous low levels after volcanic eruptions takes approximately 10 years (Chazette
834 et al., 1995; Sun et al., 2019). This further indicates the efficiency of our data capturing the volcanic
835 eruption emission features.

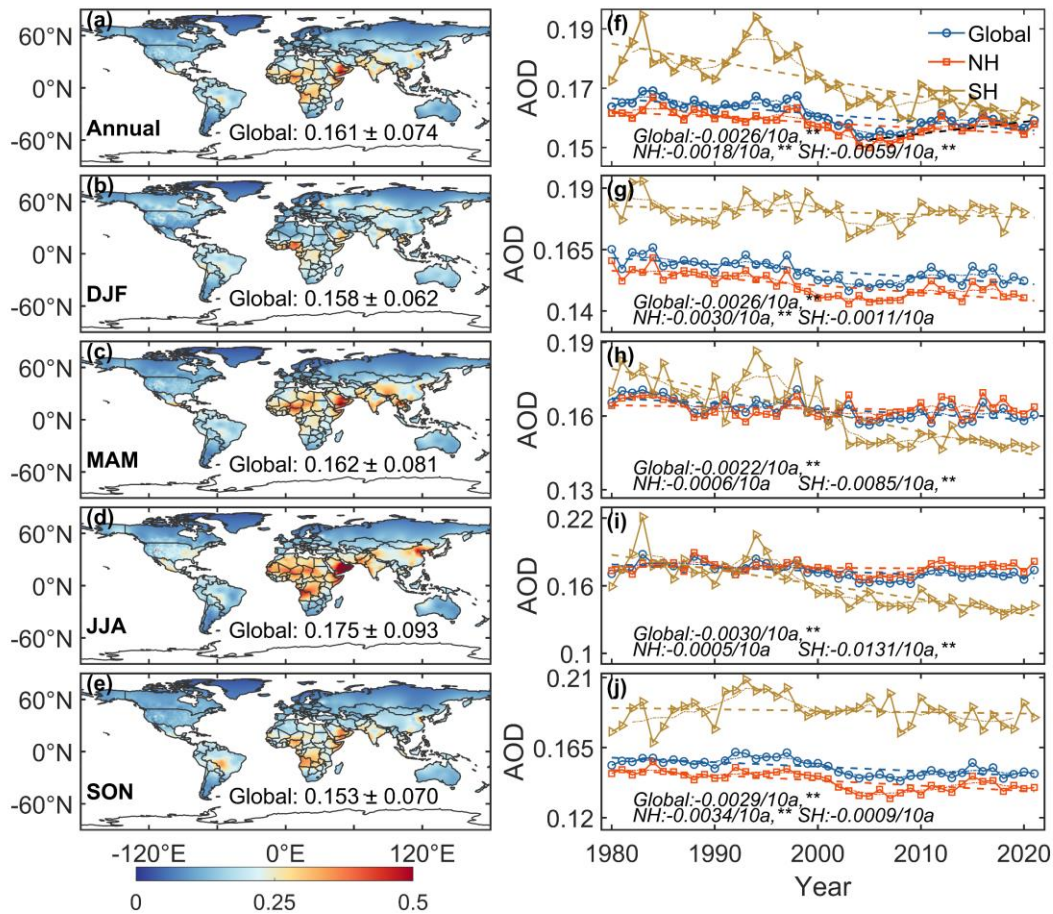
836 Due to the influence of geography, atmospheric circulation, population, and emissions, the trend of
837 global aerosols varies in different latitude Figure 14 illustrates the multi-year average AOD in
838 different latitude ranges for land, the NH, and the SH from 1980 to 2021. Within $[-20, 20^\circ N]$, the
839 global average AOD reaches its maximum (0.234), and the maximum AOD NH is 0.256 in $[0, 20^\circ N]$.
840 The highest AOD in SH is 0.217 in $[-15, 0^\circ N]$. The average AOD in SH rapidly decreases from $-$
841 $15^\circ N$ to $-35^\circ N$. In NH, AOD is generally greater than in SH from $5^\circ N$ to $65^\circ N$. When, the latitude
842 is greater than $70^\circ N$, the NH's AOD is smaller than the SH's, which may be related to low emission
843 intensity and low population density in high latitude areas.

844 The seasonal trends of AOD during 1980-2021 at the global and hemispheric scales are shown in
845 Figure 13 (g-j). The global AOD shows a decreasing trend in all seasons ($-0.002 \sim -0.003/10a$). The
846 large declining trends are observed in JJA and SON, with decreasing trend values of $-0.003/10a$ and $-$
847 $0.0029/10a$, respectively. DJF and MAM follow with decreasing trend values of $-0.0026/10a$ and $-$
848 $0.0022/10a$, respectively, all passing the significance test ($p < 0.01$). For the NH, the AOD trends in
849 different seasons are $-0.0030/10a$ (DJF), $-0.0006/10a$ (MAM), $-0.0005/10a$ (JJA), and $-0.0034/10a$
850 (SON). DJF and SON pass the significance test ($p < 0.01$), while MAM and JJA do not. In the SH,
851 the trends are as follows: $-0.0011/10a$ (DJF), $-0.0085/10a$ (MAM), $-0.0131/10a$ (JJA), and $-$
852 $0.0009/10a$ (SON). Interestingly, in contrast to the NH, MAM and JJA pass the significance test,
853 while DJF and SON do not. The largest declining season in the NH is winter, while in the SH, it is
854 summer. The decreasing trend in the SH is more than four times greater than that in the NH,
855 particularly before the year 2000. While both the global and SH AOD exhibit a decreasing trend
856 since 2005, the NH has shown a significant increase in winter AOD, leading to an overall increasing

857 trend. Moreover, the NH shows an increasing trend of 0.004/10a from 2005 to 2021.

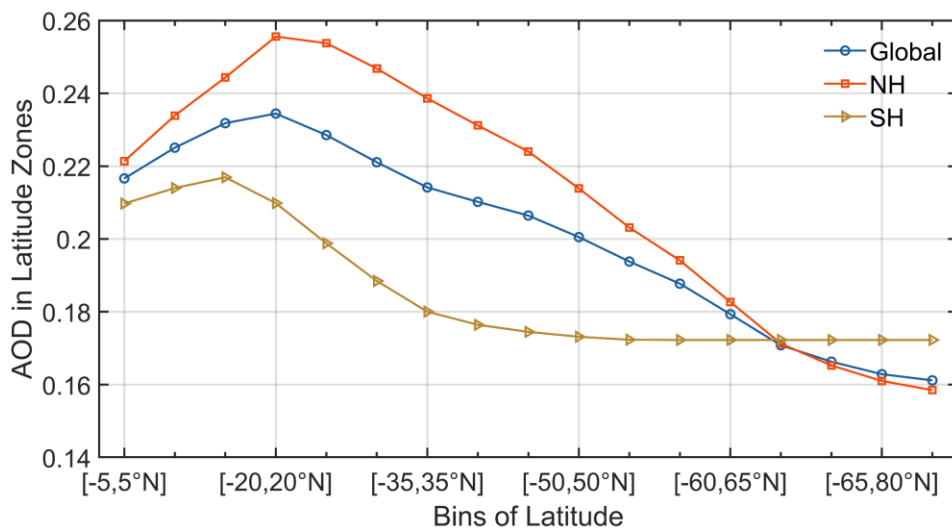
858 Annual SO₂ emissions increased from 9.4 to 15.3 TgS from 2000 to 2005, which ultimately ended
 859 up as sulfate aerosols, leading to a significant increase in sulfate aerosols (Hofmann et al., 2009).
 860 More relevantly, the frequent volcanic eruptions in tropical regions from 2002 to 2006, combined
 861 with seasonal circulation patterns during winter, led to the transport of aerosol particles to higher
 862 latitudes (Hofmann et al., 2009; Vernier et al., 2011; Sawamura et al., 2012; Andersson et al., 2015).

863



864

865 **Figure 13:** The multi-year averages of VIS_AOD from 1980 to 2021. Global land (circle), northern
 866 hemisphere (NH,0-85°N) (triangle) and southern hemisphere (SH,0-60°S) (square) annual and
 867 seasonal AOD. The symbol, **, represents that the test passed at a significance level of 0.01. DJF
 868 represents December and next January and February. MAM represents March, April, and May. JJA
 869 represents June, July, and August. SON represents September, October, and November.



870

871 **Figure 14:** The global land (blue), northern hemisphere's (red) and southern hemisphere's (yellow)
 872 multi-year average VIS_AOD from 1980 to 2021 in different latitude zones. The latitude range is
 873 from -60 to 85°N, with a bin of 5°.

874 **3.6 Interannual variability and trend of visibility-derived AOD over regions**

875 The distribution of AOD over global land exhibits significant spatial heterogeneity. Large variations
 876 in aerosol concentrations exist among different regions, leading to a non-uniform spatial distribution
 877 of AOD globally. Accurately assessing the long-term trends of aerosol loading is a key for
 878 quantifying aerosol climate change, and it is crucial for evaluating the effectiveness of measures
 879 implemented to improve regional air quality and reduce anthropogenic aerosol emissions.

880 To analyze the spatiotemporal characteristics and trends of AOD in different regions, we selected
 881 12 representative regions that are influenced by various aerosol sources(Wang et al., 2009; Hsu et
 882 al., 2012; Chin et al., 2014), such as desert, industry, anthropogenic emissions, and biomass burning
 883 emissions, which nearly cover the most land and are densely populated regions (Kummu et al.,
 884 2016). These representative regions are Eastern Europe, Western Europe, Western North America,
 885 Eastern North America, Central South America, Western Africa, Southern Africa, Australia,
 886 Southeast Asia, Northeast Asia, Eastern China, and India, as shown in Figure 1. We use multi-year
 887 average and seasonal average AOD to evaluate aerosol loadings (Figure 15), the annual average of
 888 monthly anomalies to analyze interannual trends (Figure 16), and the seasonal average to analyze
 889 seasonal trends (Figure 17) in 12 regions from 1980 to 2021.

890 We can see some differences between VIS_AOD and MODIS AOD. In addition to model errors,
 891 the spatial matching between meteorological stations and MODIS, terrain, surface coverage, and
 892 station altitude will also bring errors. When particle transport and photochemical reactions occur
 893 above the boundary layer, visibility cannot capture the feature, which will also increase the
 894 uncertainty. However, bias is inevitable and can only be kept as small as possible. From the trend,
 895 they have similar changing characteristics, especially on monthly and yearly scales.

896 Figure 15 shows the regions with high AOD level from 1980 to 2021 (multi-year average AOD >
 897 0.2) are in West Africa, Northeast Asia, Eastern China, and India. The AOD values in Eastern North

898 America, Central South America, South Africa, and Southeast Asia range from 0.15 to 0.2. The
899 AOD values in Eastern Europe, Western Europe, Western North America, and Australia are less than
900 0.15.

901 Europe is an industrial region with a low aerosol loading region, and the multi-year average AOD
902 in Eastern Europe (0.144 ± 0.007) is higher than that in Western Europe (0.139 ± 0.003) during 1980-
903 2021. Eastern Europe shows a greater downward trend in AOD ($-0.0041/10a$) compared to Western
904 Europe ($-0.0021/10a$). The highest AOD is observed in JJA, the dry period when solar irradiation
905 and boundary layer height increase, with Eastern Europe at 0.161 and Western Europe at 0.162,
906 which could be due to increases in secondary aerosols, biomass burning, and dust transport from
907 the Sahara (Mehta et al., 2016). However, there are seasonal variations. In Eastern Europe, the
908 seasonal AOD ranking from high to low is JJA (0.161) > DJF (0.147) > MAM (0.138) > SON
909 (0.131), while in Western Europe, it is JJA (0.162) > MAM (0.140) > SON (0.136) > DJF (0.117).
910 The differences among seasons are larger in Western Europe. AOD in Eastern Europe shows
911 declining trends in all seasons, while it does not pass the significance test in MAM. Among four
912 seasons, SON has the largest decline trend of AOD ($-0.0058/10a$). In Western Europe, DJF, JJA, and
913 SON exhibit declining trends of AOD that pass the significance test, while the MAM shows a
914 significant increase trend of AOD ($0.0022/10a$), which may be due to eruptions of the
915 Eyjafjallajökull volcano in Iceland in spring 2010 (Karbowska and Zembrzuski, 2016). Both
916 Western and Eastern Europe experienced increasing trends in AOD during the period of 1995-2005,
917 with Western Europe showing a greater increase. However, after 2000, the decline rate accelerated
918 in both regions. The downward trend in Europe is attributed to the reduction of biomass burning,
919 anthropogenic aerosols, and aerosol precursors (such as sulfur dioxide)(Wang et al., 2009; Chin et
920 al., 2014; Mortier et al., 2020).

921 North America is also an industrial region with a low aerosol loading. The average AOD values for
922 Eastern and Western North America during 1980-2021 are 0.153 ± 0.004 and 0.131 ± 0.005 ,
923 respectively, with the Eastern region being higher than the Western region by 0.022. From 1980 to
924 2021, both Eastern ($-0.0021/10a$) and Western North America ($-0.0009/10a$) show a downward trend;
925 however, the decline in the Western region is not statistically significant. And the trend is -
926 $0.0172/10a$ from 1995 to 2005 and $0.0096/10a$ from 2005 to 2021. The average AOD values in DJF,
927 MAM, JJA, and SON in Western North America are 0.1367, 0.1286, 0.1457, and 0.114, respectively,
928 compared to 0.137, 0.145, 0.1913, and 0.138 in Eastern North America. The lowest AOD values of
929 12 regions during DJF and SON are observed in Western North America (Remer et al., 2008).
930 Specifically, in the Western region, there is a consistent increasing trend during MAM ($0.004/10a$)
931 from 1980 to 2021, while JJA and SON also show an increase after 2000, except for DJF (-
932 $0.0032/10a$). In contrast, the AOD trends in the Eastern region remain unchanged during the period
933 1980-2021, except for MAM, which shows a stable increasing trend ($0.0033/10a$), while DJF, JJA,
934 and SON exhibit decreasing trends ($-0.0023/10a$, $-0.0040/10a$, $-0.0053/10a$, respectively). In the
935 Western region, the annual mean AOD started to increase after 2005, while in the Eastern region,
936 the increase was not significant. The upward trend may be due to low rainfall and increased wildfire
937 activities (Yoon et al., 2014). The decrease in AOD in Eastern North America is related to the
938 reduction of sulfate and organic aerosols, as well as the decrease in anthropogenic emissions caused
939 by environmental regulations (Mehta et al., 2016).

940 Central South America is a relatively high aerosol loading region, sourced from biomass burning,
941 especially in SON (Remer et al., 2008; Mehta et al., 2016), with a multi-year average AOD of
942 0.192 ± 0.017 . There is a clear downward trend ($-0.0100/10a$) from 1980 to 2021, which is slightly
943 greater than the trend ($-0.0090/10a$) from 1998 to 2010 (Hsu et al., 2012) and AOD decreased from
944 1980 to 2006 (Streets et al., 2009) and from 2001 to 2014 (Mehta et al., 2016). Although DJF (0.199)
945 and SON (0.226) have higher values compared to MAM (0.180) and JJA (0.163), the large declining
946 trends are observed in MAM ($-0.0126/10a$) and JJA ($-0.0167/10a$). It indicates that although AOD
947 has decreased overall, the aerosol loading caused by seasonal deforestation and biomass combustion
948 is still large (Mehta et al., 2016).

949 Africa is also one of the regions with a high aerosol loading worldwide. In West Africa, the average
950 AOD is 0.275 ± 0.012 during 1980-2021, and the annual AOD shows a downward trend ($-0.0008/10a$,
951 $p > 0.05$). The world's largest desert (Sahara Desert) is in West Africa, with much dust aerosol
952 discharged. AOD values in all seasons are above 0.25, with JJA (0.301) and MAM (0.300) reaching
953 0.3, and DJF and SON being 0.252 and 0.250, respectively. The AOD in DJF ($-0.0135/10a$, $p < 0.01$)
954 and SON ($-0.0026/10a$, $p > 0.05$) exhibit decreasing trends, while JJA ($0.0088/10a$, $p < 0.01$) and MAM
955 ($0.0037/10a$, $p > 0.05$) show an opposite trend. The multi-year average AOD in South Africa is
956 0.177 ± 0.020 , lower than that of West Africa. The annual mean AOD in South Africa shows a
957 significant decrease ($-0.0096/10a$). The AOD values range from 0.12 to 0.2 during 2000-2009,
958 dominated by fine particle matter from industrial pollution from biomass and fossil fuel combustion
959 (Hersey et al., 2015). The average AOD values in DJF, MAM, JJA, and SON are 0.189, 0.162, 0.147,
960 and 0.210, respectively. JJA ($-0.0268/10a$, $p < 0.01$), MAM ($-0.0126/10a$, $p < 0.01$) and SON ($-$
961 $0.0001/10a$, $p > 0.05$) exhibit a downward AOD trend, while DJF ($0.0006/10a$, $p > 0.05$) shows an
962 upward trend. AERONET and simulation results also show a decreasing trend of AOD (Chin et al.,
963 2014).

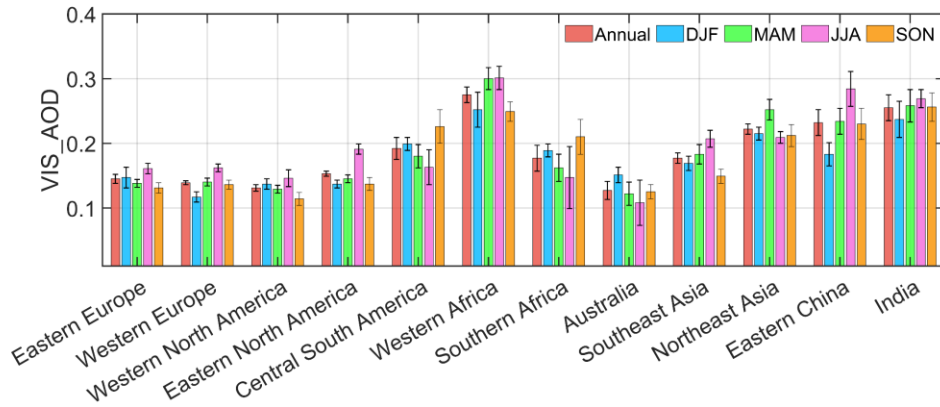
964 Australia is a region with a low aerosol loading. The multi-year mean AOD is 0.127 ± 0.014 during
965 1980-2021. The AOD ranges from 0.05 to 0.15 from AERONET during 2000-2021, and dust and
966 biomass burning are important contributors to the aerosol loading (Yang et al., 2021a). There is a
967 downward trend of AOD ($-0.0081/10a$, $p < 0.01$), which may be related to a decrease in dust and
968 biomass burning (Yoon et al., 2016; Yang et al., 2021a). In addition, research has shown that the
969 forest area in Australia has increased sharply since 2000 (Giglio et al., 2013), surpassing the forest
970 fire area of the past 14 years. The seasonal average of AOD in MAM, JJA, SON, and DJF are 0.122,
971 0.108, 0.125, and 0.151. The AOD in JJA is the lowest among all seasons and regions. The highest
972 AOD is in DJF with an increasing trend ($0.0056/10a$, $p < 0.01$), while the trends during MAM, JJA
973 and SON are $-0.0096/10a$ ($p < 0.01$), $-0.0231/10a$ ($p < 0.01$) and $-0.0042/10a$ ($p < 0.01$), respectively.
974 Ground-based observations and satellite retrievals indicate that wildfires, biomass burning and
975 sandstorms lead to high AOD in DJF and SON. The low AOD of MAM and JJA is due to a decrease
976 in the frequency of sandstorms and wildfires and an increase in precipitation (Gras et al., 1999; Yang
977 et al., 2021a; Yang et al., 2021b).

978 Asia is also a high aerosol loading area with various sources. In Southeast Asia, the multi-year
979 average AOD is 0.177 during 1980-2021 with a downward trend of AOD ($-0.0003/10a$, $p > 0.05$). It
980 is also a biomass-burning area. The seasonal average AOD ranking from high to low is JJA (0.207) >
981 MAM (0.183) > DJF (0.169) > SON (0.149). The trends in DJF ($-0.0035/10a$, $p < 0.05$), JJA ($-$
982 $0.0007/10a$, $p > 0.05$) and SON ($-0.0021/10a$, $p > 0.05$) are opposite to MAM ($0.0050/10a$, $p < 0.01$).

983 Southeast Asia has no clear long-term trend in estimated AOD or observed surface solar radiation
984 (Streets et al., 2009). In Northeast Asia, the multi-year average AOD is 0.222 during 1980-2021,
985 with no significant temporal trend. The seasonal AOD values are 0.252 in MAM, 0.215 in DJF,
986 0.212 in SON and 0.209 in JJA. AOD in MAM is significantly higher than other seasons, which
987 may be related to sandstorms in East Asia, and the reason for the high AOD in winter may be related
988 to the transportation. The trends of AOD in DJF ($-0.0025/10a$, $p>0.05$), MAM ($0.0031/10a$, $p>0.05$),
989 JJA (0) and SON ($-0.0006/10a$, $p>0.05$) are not significant. In Eastern China, the multi-year average
990 AOD is 0.233, with an increasing trend ($0.0071/10a$, $p<0.01$). The trend is $0.0151/10a$ from 1980 to
991 2006 and $-0.0469/10a$ from 2006 to 2021. The seasonal average AOD ranking from high to low is
992 JJA (0.284), MAM (0.234), SON (0.230) and DJF (0.183). The AOD trends in DJF ($0.0093/10a$,
993 $p<0.01$), MAM ($0.0092/10a$, $p<0.01$), JJA ($0.0038/10a$, $p>0.05$) and SON ($0.0065/10a$, $p<0.05$)
994 are all positive but the trend in JJA does not pass the significance test. We can see that there are three
995 stages of changes in AOD: 1980-2005, 2006-2013 and 2014-2021. In the first stage, AOD increased
996 steadily. In the second stage, AOD maintained a larger positive anomaly accompanied by
997 oscillations. The third stage experienced a rapid decline, reaching the level of the 1980s by 2021.
998 The increasing trend of AOD before 2006 may be due to the significant increase in industrial activity,
999 and after 2013, the significant decrease is closely related to the implementation of air quality-related
1000 laws and regulations, along with adjustments in the energy structure (Hu et al., 2018; Cherian and
1001 Quaas, 2020).

1002 India is a high aerosol loading area. The multi-year average AOD is 0.255, with an upward trend
1003 ($0.0096/10a$, $p<0.01$) from 1980 to 2021. Dust and biomass burning has an influence on AOD level.
1004 There are three stages: 1980-1997 ($0.0032/10a$, $p<0.01$), 1997-2005 ($-0.0420/10a$, $p<0.01$), 2005-
1005 2021 ($0.0481/10a$, $p<0.01$). Although the trend is downward in the second stage, the larger positive
1006 trend is in the third stage. The seasonal average AOD values are 0.237 in DJF, 0.258 in MAM, 0.269
1007 in JJA, and 0.256 in SON. The largest AOD is in JJA. In winter and autumn, it is affected by biomass
1008 burning, and in spring and summer, it is also affected by dust, transported from the Sahara under
1009 during the monsoon period (Remer et al., 2008). The trends in DJF ($0.0152/10a$, $p<0.01$), MAM
1010 ($0.0091/10a$, $p<0.01$), JJA ($0.0025/10a$, $p>0.05$), and SON ($0.0107/10a$, $p<0.05$) are positive. There
1011 largest trend is in winter.

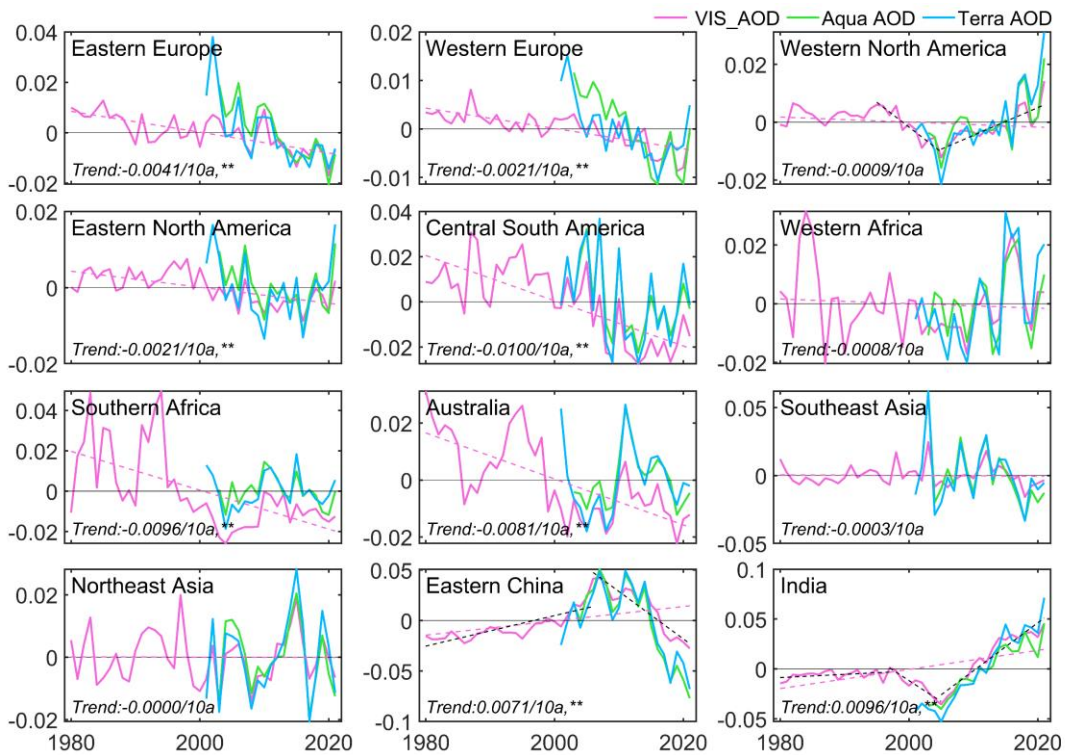
1012 To summarize, there are significant differences in the spatial distribution, annual trends, and
1013 seasonal trends of AOD across different regions from 1980 to 2021. The high aerosol loadings from
1014 1980 to 2021 are in West Africa, India and Asia, and low aerosol loading regions are in Europe,
1015 Western North America, and Australia. Eastern China and India show an increasing trend, Southeast
1016 Asia and Northeast Asia show no significant trend, and the other regions show downward trends.
1017 However, not all regional seasonal trends are consistent with their annual trends. The results in this
1018 study have supplemented the long-term trend and distribution of AOD over land.



1019

1020 **Figure 15:** Annual and seasonal averages of AOD in 12 regions during 1980-2021.

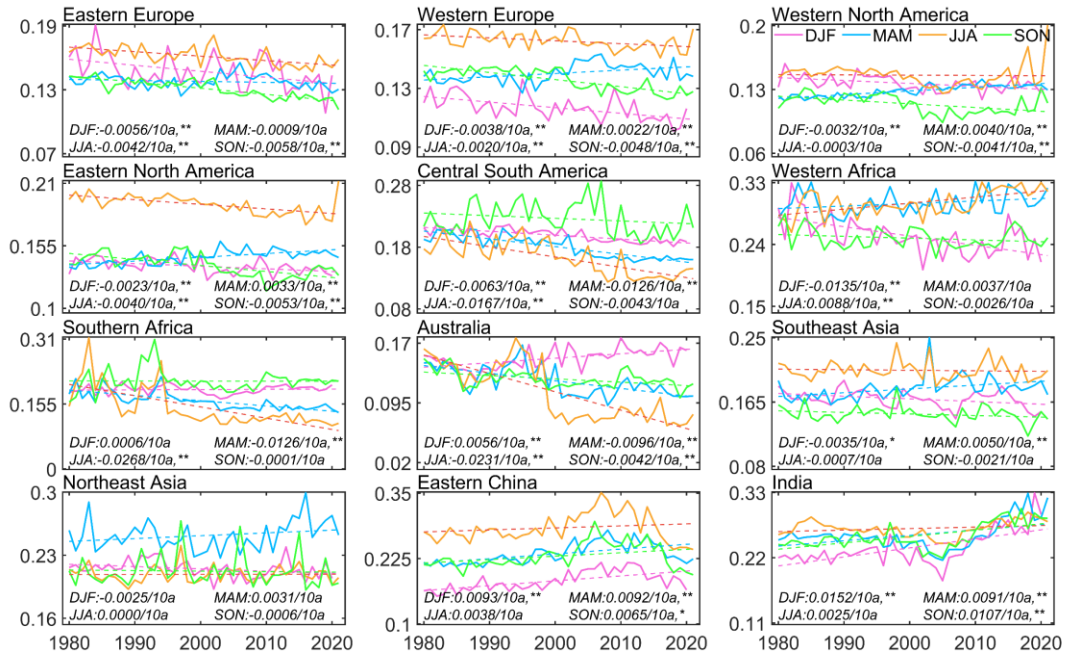
1021



1022

1023 **Figure 16:** Annual averages of monthly anomaly gridded VIS_AOD (pink line), Aqua (green line),
 1024 and Terra (blue line) MODIS AOD in 12 regions. The dotted line is the trend line.

1025



1026

1027 **Figure 17:** Seasonal averages of gridded VIS_AOD during 1980 to 2021 in 12 regions (Eastern
 1028 Europe, Western Europe, Western North America, Eastern North America, Central South America,
 1029 Western Africa, Southern Africa, Australia, Southeast Asia, Northeast Asia, Eastern China, and
 1030 India). The dotted line is the trend line.

1031 4 Data availability

1032 The visibility-derived AOD at station and grid scales over global land are available at National
 1033 Tibetan Plateau / Third Pole Environment Data Center,
 1034 <https://doi.org/10.11888/Atmos.tpsc.300822> (Hao et al., 2023).

1035 We provide the station-scale AOD from 1959 to 2021. Due to a small number and sparse
 1036 meteorological stations prior to 1980, we only provide the gridded AOD from 1980 to 2021. In order
 1037 to keep consistency in time scale, the time range we describe in this study is from 1980 to 2021. The
 1038 following is a description to the station and gridded VIS_AOD dataset.

1039 The station-scale AOD files are in ‘Station_Daily_AOD_1959_2021.zip’. The station-scale AOD
 1040 files can be directly opened by a text program (such as Notepad). The details station information is
 1041 in the file of ‘0A0A-Station_ In Information.txt’. There are eight columns in each text file, separated
 1042 by commas and column names are Datetime, TEMP (°C), DEW (°C), RH (%), WS (m/s), SLP (hPa),
 1043 DRYVIS (km), and VIS_AOD (550nm). The 2-7th column names are temperature (unit: °C), dew
 1044 temperature (unit: °C), relative humidity (unit: %), wind speed (unit: m/s), sea level pressure (unit:
 1045 hPa), and dry visibility (unit: km).

1046 The gridded AOD is in the file of ‘Gridded_Monthly_AOD_1980_2021.nc’ with a NETCDF4
 1047 format. There are three variables: ‘VIS_AOD’ (AOD derived from visibility), ‘W95CI’ (the width
 1048 of the 95% confidence interval), and ‘QA_FLAG’ (quality flag for VIS_AOD). We classify the
 1049 quality of VIS_AOD into three levels based on ‘W95CI’: (1) High quality (QA_FLAG=1);

1050 W95CI \leq 0.03; (2) Medium quality (QA_FLAG=2), 0.03<W95CI \leq 0.06; and Low quality
1051 (QA_FLAG=3), W95CI>0.06. The more details are in '0A0B-ReadMe.txt'.

1052 **5 Conclusions**

1053 In this study, we employ a machine learning technique to derive AOD for over 5000 land stations
1054 worldwide, based on satellite data, visibility, and related meteorological variables. The target is
1055 Aqua MODIS AOD. Monthly AOD is interpolated into a 0.5° grid using ordinary kriging with area
1056 weighting. The accuracy and performance of the derived AOD are assessed and validated against
1057 Terra MODIS AOD as well as AERONET ground-based observations and MRRRA-2 AOD. The
1058 gridded AOD is evaluated by Aqua and Terra MODIS AOD and a 95% confidence interval is
1059 calculated. We obtain daily AOD (550nm) at 5032 global land stations from 1980 to 2021, as well
1060 as monthly gridded AOD. The two datasets complement the shortcomings of AOD data in terms of
1061 time scale and spatial coverage. Finally, the spatiotemporal variation in AOD is analyzed for global
1062 land, the Southern Hemisphere, the Northern Hemisphere, and 12 regions in the past 42 years.
1063 Several key findings have been given in this study as follows.

1064 **1. Modeling and gridding evaluation.** The mean RMSE, MAE, and R of all stations are 0.078,
1065 0.044, and 0.750, respectively. The RMSE of 93% stations is less than 0.11, the MAE of 91% is less
1066 than 0.06, and the R of 88% is greater than 0.7, respectively. Compared to Aqua and Terra, the
1067 average biases of gridded AOD are 3.3% and 1.9%, and the spatial correlation coefficients are 0.80
1068 and 0.79, with the zonal correlation coefficients of 0.99 and 0.99 and the meridional correlation
1069 coefficients of 0.99 and 0.90.

1070 **2. Model validation.** For the daily scale, the R, RMSE and MAE of between VIS_AOD and Aqua
1071 AOD is 0.799, 0.079 and 0.044, respectively. The percentage of sample point falling within the EE
1072 envelopes is 84.12%. The R between VIS_AOD and Terra AOD is 0.542, with a RMSE of 0.125
1073 and MAE of 0.078. The percentage falling within the EE envelopes is 64.76%. The R between
1074 VIS_AOD and AERONET AOD is 0.546, with a RMSE of 0.186 and MAE of 0.099. The percentage
1075 falling within the EE envelopes is 57.87%. For the monthly and annual scales, RMSE and MAE
1076 show a significant decrease between VIS_AOD and Aqua, Terra, and AERONET AOD, and R and
1077 percentages falling within EE show a significant increase.

1078 **3. Error analysis.** The average bias is 0.015 (AOD < 0.1), with 83% of data within the EE envelopes.
1079 As pollution level increases, the negative mean bias becomes significant and the underestimation
1080 increases. There is a negative bias in the low elevation (\leq 0.5km) with a percentage of 60%-64%
1081 falling within the EE envelopes and a positive bias in high elevation (0.5-1.2km) with a percentage
1082 of 50%-65% falling within the EE envelopes. The elevation of AERONET's site caused a bias in
1083 high elevation. When the elevation difference is negative (the elevation of the meteorological station
1084 is lower than that of the AERONET site), there is a significant positive bias. When the difference is
1085 positive, the mean bias approaches 0 or is positive. The bias does not change significantly with
1086 increasing distance between the meteorological station and AERONET site.

1087 **4. Global land AOD.** The global, NH, and SH AOD values from 1980 to 2021 are 0.161 ± 0.074 ,
1088 0.158 ± 0.076 , and 0.173 ± 0.059 , respectively. Trends in AOD for the global, NH, and SH
1089 demonstrate a decreasing trend of $-0.0026/10a$, $-0.0018/10a$, and $-0.0059/10a$, respectively ($p < 0.01$).

1090 The seasonal AOD ranking from high to low is JJA>MAM>DJF>SON over the global land and in
1091 the NH, while in the SH, it is DJF>JJA>MAM>SON. The largest declining trends are observed in
1092 NH summer and SH winter.

1093 **5. Regional AOD.** From 1980 to 2021, regions with high aerosol loadings ($AOD > 0.2$) were found
1094 in West Africa, Northeast Asia, Eastern China, and India. Regions with moderate aerosol loadings
1095 (AOD between 0.15 and 0.2) are Eastern North America, Central South America, South Africa, and
1096 Southeast Asia. Eastern Europe, Western Europe, Western North America, and Australia are regions
1097 with low aerosol loadings ($AOD < 0.15$). The trends are $-0.0041/10a$, $-0.0021/10a$, $-0.0009/10a$, $-$
1098 $0.0021/10a$, $-0.0100/10a$, $-0.0008/10a$, $-0.0096/10a$, $-0.0081/10a$, $-0.0003/10a$, $-0.0000/10a$, $-$
1099 $0.0071/10a$, and $0.0096/10a$ in Eastern Europe, Western Europe, Western North America, Eastern
1100 North America, Central South America, Western Africa, Southern Africa, Australia, Southeast Asia,
1101 Northeast Asia, Eastern China, and India, respectively.

1102 **Competing interests**

1103 The contact author has declared that none of the authors has any competing interests.

1104 **Acknowledgments**

1105 This work is supported by the National Key Research & Development Program of China
1106 (2022YFF0801302) and the National Natural Science Foundation of China (41930970). The hourly
1107 visibility data are downloaded from <https://mesonet.agron.iastate.edu/ASOS>. The Aerosol Robotic
1108 Network (AERONET) 15-minute aerosol optical depth (AOD) data are downloaded from which
1109 can be downloaded from <https://aeronet.gsfc.nasa.gov>. The MODIS AOD data are downloaded from
1110 <https://ladsweb.modaps.eosdis.nasa.gov>.

1111

1112 **References**

1113 Ackerman, A. S., Hobbs, P. V., and Toon, O. B.: A model for particle microphysics, turbulent mixing,
1114 and radiative transfer in the stratocumulus-topped marine boundary layer and comparisons with
1115 measurements, *J. Atmos. Sci.*, 52, 1204-1236, [https://doi.org/10.1175/1520-0469\(1995\)052<1204:AMFPMT>2.0.CO;2](https://doi.org/10.1175/1520-0469(1995)052<1204:AMFPMT>2.0.CO;2), 1995.
1116
1117 Albrecht, B. A.: Aerosols, cloud microphysics, and fractional cloudiness, *Science*, 245, 1227-1230,
1118 <https://doi.org/10.1126/science.245.4923.1227>, 1989.
1119 Anderson, T. L., Charlson, R. J., Bellouin, N., Boucher, O., Chin, M., Christopher, S. A., Haywood, J.,
1120 Kaufman, Y. J., Kinne, S., Ogren, J. A., Remer, L. A., Takemura, T., Tanre, D., Torres, O., Trepte, C. R.,
1121 Wielicki, B. A., Winker, D. M., and Yu, H. B.: An "A-Train" strategy for quantifying direct climate
1122 forcing by anthropogenic aerosols, *B. Am. Meteorol. Soc.*, 86, 1795-+, <https://doi.org/10.1175/Bams-86-12-1795>, 2005.
1123
1124 Andersson, S. M., Martinsson, B. G., Vernier, J.-P., Friberg, J., Brenninkmeijer, C. A., Hermann, M., Van
1125 Velthoven, P. F., and Zahn, A.: Significant radiative impact of volcanic aerosol in the lowermost
1126 stratosphere, *Nat. Commun.*, 6, 7692, <https://doi.org/10.1038/ncomms8692>, 2015.

1127 Andrews, E., Sheridan, P. J., Ogren, J. A., Hageman, D., Jefferson, A., Wendell, J., Alástuey, A., Alados-
1128 Arboledas, L., Bergin, M., and Ealo, M.: Overview of the NOAA/ESRL federated aerosol network, B.
1129 Am. Meteorol. Soc., 100, 123-135, <https://doi.org/10.1175/BAMS-D-17-0175.1>, 2019.

1130 Bergstrom, R. W., Pilewskie, P., Russell, P. B., Redemann, J., Bond, T. C., Quinn, P. K., and Sierau, B.:
1131 Spectral absorption properties of atmospheric aerosols, Atmos. Chem. Phys., 7, 5937-5943,
1132 <https://doi.org/10.5194/acp-7-5937-2007>, 2007.

1133 Berk, R. A.: Classification and Regression Trees (CART), in: Statistical Learning from a Regression
1134 Perspective, Springer New York, New York, NY, 1-65, https://doi.org/10.1007/978-0-387-77501-2_3,
1135 2008.

1136 Bescond, A., Yon, J., Girasole, T., Jouen, C., Rozé, C., and Coppalle, A.: Numerical investigation of the
1137 possibility to determine the primary particle size of fractal aggregates by measuring light depolarization,
1138 J. Quant. Spectrosc. Ra., 126, 130-139, <https://doi.org/10.1016/j.jqsrt.2012.10.011>, 2013.

1139 Boers, R., van Weele, M., van Meijgaard, E., Savenije, M., Siebesma, A. P., Bosveld, F., and Stammes,
1140 P.: Observations and projections of visibility and aerosol optical thickness (1956-2100) in the
1141 Netherlands: impacts of time-varying aerosol composition and hygroscopicity, Environ. Res. Lett., 10,
1142 <https://doi.org/10.1088/1748-9326/10/1/015003>, 2015.

1143 Bokoye, A. I., Royer, A., O'Neil, N., Cliche, P., Fedosejevs, G., Teillet, P., and McArthur, L.:
1144 Characterization of atmospheric aerosols across Canada from a ground-based sunphotometer network:
1145 AEROCAN, Atmos. Ocean, 39, 429-456, <https://doi.org/10.1080/07055900.2001.9649687>, 2001.

1146 Bösenberg, J. and Matthias, V.: EARLINET: A European Aerosol Research Lidar Network to Establish
1147 an Aerosol Climatology, Max Planck Institut Fur Meteorologie, 2003.

1148 Bright, J. M. and Gueymard, C. A.: Climate-specific and global validation of MODIS Aqua and Terra
1149 aerosol optical depth at 452 AERONET stations, Sol. Energy, 183, 594-605,
1150 <https://doi.org/10.1016/j.solener.2019.03.043>, 2019.

1151 Browne, M. W.: Cross-validation methods, J. Math. Psychol., 44, 108-132,
1152 <https://doi.org/10.1006/jmps.1999.1279>, 2000.

1153 Calvo, A. I., Alves, C., Castro, A., Pont, V., Vicente, A. M., and Fraile, R.: Research on aerosol sources
1154 and chemical composition: Past, current and emerging issues, Atmos. Res., 120, 1-28,
1155 <https://doi.org/10.1016/j.atmosres.2012.09.021>, 2013.

1156 Chafe, Z. A., Brauer, M., Klimont, Z., Van Dingenen, R., Mehta, S., Rao, S., Riahi, K., Dentener, F., and
1157 Smith, K. R.: Household Cooking with Solid Fuels Contributes to Ambient PM_{2.5} Air Pollution and the
1158 Burden of Disease, Environ. Health Persp., 122, 1314-1320, <https://doi.org/10.1289/ehp.1206340>, 2014.

1159 Chazette, P., David, C., Lefrère, J., Godin, S., Pelon, J., and Mégie, G.: Comparative lidar study of the
1160 optical, geometrical, and dynamical properties of stratospheric post-volcanic aerosols, following the
1161 eruptions of El Chichon and Mount Pinatubo, J. Geophys. Res-Atmos., 100, 23195-23207,
1162 <https://doi.org/10.1029/95JD02268>, 1995.

1163 Che, H., Zhang, X., Chen, H., Damiri, B., Goloub, P., Li, Z., Zhang, X., Wei, Y., Zhou, H., Dong, F., Li,
1164 D., and Zhou, T.: Instrument calibration and aerosol optical depth validation of the China Aerosol Remote
1165 Sensing Network, J. Geophys. Res-Atmos., 114, <https://doi.org/10.1029/2008jd011030>, 2009.

1166 Che, H., Xia, X., Zhu, J., Li, Z., Dubovik, O., Holben, B., Goloub, P., Chen, H., Estelles, V., Cuevas-
1167 Agullo, E., Blarel, L., Wang, H., Zhao, H., Zhang, X., Wang, Y., Sun, J., Tao, R., Zhang, X., and Shi, G.:
1168 Column aerosol optical properties and aerosol radiative forcing during a serious haze-fog month over
1169 North China Plain in 2013 based on ground-based sunphotometer measurements, Atmos. Chem. Phys.,
1170 14, 2125-2138, <https://doi.org/10.5194/acp-14-2125-2014>, 2014.

1171 Chen, A., Zhao, C., and Fan, T.: Spatio-temporal distribution of aerosol direct radiative forcing over mid-
1172 latitude regions in north hemisphere estimated from satellite observations, *Atmos. Res.*, 266, 105938,
1173 <https://doi.org/10.1016/j.atmosres.2021.105938>, 2022.

1174 Chen, D., Ou, T., Gong, L., Xu, C.-Y., Li, W., Ho, C.-H., and Qian, W.: Spatial Interpolation of Daily
1175 Precipitation in China: 1951-2005, *Adv. Atmos. Sci.*, 27, 1221-1232, <https://doi.org/10.1007/s00376-010-9151-y>, 2010.

1176
1177 Cherian, R. and Quaas, J.: Trends in AOD, clouds, and cloud radiative effects in satellite data and CMIP5
1178 and CMIP6 model simulations over aerosol source regions, *Geophys. Res. Lett.*, 47, e2020GL087132,
1179 <https://doi.org/10.1029/2020GL087132>, 2020.

1180 Chin, M., Diehl, T., Tan, Q., Prospero, J., Kahn, R., Remer, L., Yu, H., Sayer, A., Bian, H., and
1181 Geogdzhayev, I.: Multi-decadal aerosol variations from 1980 to 2009: a perspective from observations
1182 and a global model, *Atmos. Chem. Phys.*, 14, 3657-3690, <https://doi.org/10.5194/acp-14-3657-2014>,
1183 2014.

1184 Chu, D., Kaufman, Y., Ichoku, C., Remer, L., Tanré, D., and Holben, B.: Validation of MODIS aerosol
1185 optical depth retrieval over land, *Geophys. Res. Lett.*, 29, MOD2-1-MOD2-4,
1186 <https://doi.org/10.1029/2001GL013205>, 2002.

1187 Chuang, P.-J. and Huang, P.-Y.: B-VAE: a new dataset balancing approach using batched Variational
1188 AutoEncoders to enhance network intrusion detection, *J. Supercomput.*, <https://doi.org/10.1007/s11227-023-05171-w>, 2023.

1189
1190 Deuzé, J., Goloub, P., Herman, M., Marchand, A., Perry, G., Susana, S., and Tanré, D.: Estimate of the
1191 aerosol properties over the ocean with POLDER, *J. Geophys. Res-Atmos.*, 105, 15329-15346,
1192 <https://doi.org/10.1029/2000JD900148>, 2000.

1193 Dhanya, R., Paul, I. R., Akula, S. S., Sivakumar, M., and Nair, J. J.: F-test feature selection in Stacking
1194 ensemble model for breast cancer prediction, *Procedia. Comput. Sci.*, 171, 1561-1570,
1195 <https://doi.org/10.1016/j.procs.2020.04.167>, 2020.

1196 Diner, D. J., Beckert, J. C., Reilly, T. H., Bruegge, C. J., Conel, J. E., Kahn, R. A., Martonchik, J. V.,
1197 Ackerman, T. P., Davies, R., and Gerstl, S. A. W.: Multi-angle Imaging SpectroRadiometer (MISR)
1198 instrument description and experiment overview, *Ieee T. Geosci. Remote.*, 98, 1072-1087,
1199 <https://doi.org/10.1109/36.700992>, 1998.

1200 Dong, Y., Li, J., Yan, X., Li, C., Jiang, Z., Xiong, C., Chang, L., Zhang, L., Ying, T., and Zhang, Z.:
1201 Retrieval of aerosol single scattering albedo using joint satellite and surface visibility measurements,
1202 *Remote Sens. Environ.*, 294, 113654, <https://doi.org/10.1016/j.rse.2023.113654>, 2023.

1203 Dubovik, Oleg, Holben, Brent, Eck, Thomas, F., Smirnov, Alexander, and Kaufman: Variability of
1204 Absorption and Optical Properties of Key Aerosol Types Observed in Worldwide Locations, *J. Atmos.*
1205 *Sci.*, 59, 590-590, [https://doi.org/10.1175/1520-0469\(2002\)059<0590:VOAOP>2.0.CO;2](https://doi.org/10.1175/1520-0469(2002)059<0590:VOAOP>2.0.CO;2), 2002a.

1206 Dubovik, O., Smirnov, A., Holben, B. N., King, M. D., Kaufman, Y. J., Eck, T. F., and Slutsker, I.:
1207 Accuracy assessments of aerosol optical properties retrieved from Aerosol Robotic Network (AERONET)
1208 Sun and sky radiance measurements, *J. Geophys. Res-Atmos.*, 105, 9791-9806,
1209 <https://doi.org/10.1029/2000jd900040>, 2000.

1210 Dubovik, O., Holben, B., Eck, T. F., Smirnov, A., Kaufman, Y. J., King, M. D., Tanré, D., and Slutsker,
1211 I.: Variability of absorption and optical properties of key aerosol types observed in worldwide locations,
1212 *J. Atmos. Sci.*, 59, 590-608, [https://doi.org/10.1175/1520-0469\(2002\)059<0590:VOAOP>2.0.CO;2](https://doi.org/10.1175/1520-0469(2002)059<0590:VOAOP>2.0.CO;2),
1213 2002b.

1214 Eck, T. F., Holben, B. N., Reid, J. S., Sinyuk, A., Giles, D. M., Arola, A., Slutsker, I., Schafer, J. S.,

1215 Sorokin, M. G., and Smirnov, A.: The extreme forest fires in California/Oregon in 2020: Aerosol optical
1216 and physical properties and comparisons of aged versus fresh smoke, *Atmos. Environ.*, 305, 119798,
1217 <https://doi.org/10.1016/j.atmosenv.2023.119798>, 2023.

1218 Elterman, L.: Relationships between vertical attenuation and surface meteorological range, *Appl. Optics*,
1219 9, 1804-1810, <https://doi.org/10.1364/AO.9.001804>, 1970.

1220 Fan, H., Zhao, C., Yang, Y., and Yang, X.: Spatio-Temporal Variations of the
1221 PM_{2.5}/PM₁₀ Ratios and Its Application to Air Pollution Type Classification
1222 in China, *Front. Environ. Sci.*, 9, <https://doi.org/10.3389/fenvs.2021.692440>, 2021.

1223 Fernández, A., Garcia, S., Herrera, F., and Chawla, N. V.: SMOTE for learning from imbalanced data:
1224 progress and challenges, marking the 15-year anniversary, *J. Artif. Intell. Res.*, 61, 863-905,
1225 <https://doi.org/10.1613/jair.1.11192>, 2018.

1226 Forster, P., Ramaswamy, V., Artaxo, P., Bernsten, T., Betts, R., Fahey, D. W., Haywood, J., Lean, J., Lowe,
1227 D. C., and Myhre, G.: Changes in atmospheric constituents and in radiative forcing, *Climate Change*
1228 2007: The Physical Science Basis. Contribution of Working Group I to the 4th Assessment Report of the
1229 Intergovernmental Panel on Climate Change, 2007.

1230 Gelaro, R., McCarty, W., Suárez, M. J., Todling, R., Molod, A., Takacs, L., Randles, C. A., Darmenov,
1231 A., Bosilovich, M. G., Reichle, R., Wargan, K., Coy, L., Cullather, R., Draper, C., Akella, S., Buchard,
1232 V., Conaty, A., da Silva, A. M., Gu, W., Kim, G.-K., Koster, R., Lucchesi, R., Merkova, D., Nielsen, J.
1233 E., Partyka, G., Pawson, S., Putman, W., Rienecker, M., Schubert, S. D., Sienkiewicz, M., and Zhao, B.:
1234 The Modern-Era Retrospective Analysis for Research and Applications, Version 2 (MERRA-2), *J.*
1235 *Climate*, 30, 5419-5454, <https://doi.org/10.1175/JCLI-D-16-0758.1>, 2017.

1236 Giglio, L., Randerson, J. T., and Van Der Werf, G. R.: Analysis of daily, monthly, and annual burned area
1237 using the fourth-generation global fire emissions database (GFED4), *J. Geophys. Res.-Biogeo.*, 118, 317-
1238 328, <https://doi.org/10.1002/jgrg.20042>, 2013.

1239 Giles, D. M., Sinyuk, A., Sorokin, M. G., Schafer, J. S., Smirnov, A., Slutsker, I., Eck, T. F., Holben, B.
1240 N., Lewis, J. R., Campbell, J. R., Welton, E. J., Korkin, S. V., and Lyapustin, A. I.: Advancements in the
1241 Aerosol Robotic Network (AERONET) Version 3 database – automated near-real-time quality control
1242 algorithm with improved cloud screening for Sun photometer aerosol optical depth (AOD) measurements,
1243 *Atmos. Meas. Tech.*, 12, 169-209, <https://doi.org/10.5194/amt-12-169-2019>, 2019.

1244 Goovaerts, P.: Geostatistical approaches for incorporating elevation into the spatial interpolation of
1245 rainfall, *Journal of Hydrology*, 228, 113-129, [https://doi.org/10.1016/s0022-1694\(00\)00144-x](https://doi.org/10.1016/s0022-1694(00)00144-x), 2000.

1246 Gras, J., Jensen, J., Okada, K., Ikegami, M., Zaizen, Y., and Makino, Y.: Some optical properties of smoke
1247 aerosol in Indonesia and tropical Australia, *Geophys. Res. Lett.*, 26, 1393-1396,
1248 <https://doi.org/10.1029/1999GL900275>, 1999.

1249 Guerrero-Rascado, J. L., Landulfo, E., Antuña, J. C., Barbosa, H. d. M. J., Barja, B., Bastidas, Á. E.,
1250 Bedoya, A. E., da Costa, R. F., Estevan, R., and Forno, R.: Latin American Lidar Network (LALINET)
1251 for aerosol research: Diagnosis on network instrumentation, *J. Atmos. Sol-Terr. Phys.*, 138, 112-120,
1252 <https://doi.org/10.1016/j.jastp.2016.01.001>, 2016.

1253 Guo, J., Zhang, J., Yang, K., Liao, H., Zhang, S., Huang, K., Lv, Y., Shao, J., Yu, T., and Tong, B.:
1254 Investigation of near-global daytime boundary layer height using high-resolution radiosondes: first
1255 results and comparison with ERA5, MERRA-2, JRA-55, and NCEP-2 reanalyses, *Atmos. Chem. Phys.*,
1256 21, 17079-17097, <https://doi.org/10.5194/acp-21-17079-2021>, 2021.

1257 Hao, H., Wang, K., and Wu, G.: Visibility-derived aerosol optical depth over global land (1980-2021),
1258 National Tibetan Plateau Data Center [dataset], <https://doi.org/10.11888/Atmos.tpdc.300822>, 2023.

1259 He, H., Bai, Y., Garcia, E. A., and Li, S.: ADASYN: Adaptive synthetic sampling approach for
1260 imbalanced learning, IEEE World Congress on Computational Intelligence, 1322-1328,
1261 <https://doi.org/10.1109/IJCNN.2008.4633969>, 2008.

1262 Hersbach, H., Bell, B., Berrisford, P., Hirahara, S., Horányi, A., Muñoz-Sabater, J., Nicolas, J., Peubey,
1263 C., Radu, R., and Schepers, D.: The ERA5 global reanalysis, Q. J. Roy. Meteor. Soc., 146, 1999-2049,
1264 <https://doi.org/10.1002/qj.3803>, 2020.

1265 Hersey, S. P., Garland, R. M., Crosbie, E., Shingler, T., Sorooshian, A., Piketh, S., and Burger, R.: An
1266 overview of regional and local characteristics of aerosols in South Africa using satellite, ground, and
1267 modeling data, Atmos. Chem. Phys., 15, 4259-4278, <https://doi.org/10.5194/acp-15-4259-2015>, 2015.

1268 Hirono, M. and Shibata, T.: Enormous increase of stratospheric aerosols over Fukuoka due to volcanic
1269 eruption of El Chichon in 1982, Geophys. Res. Lett., 10, 152-154,
1270 <https://doi.org/10.1029/GL010i002p00152>, 1983.

1271 Hofmann, D., Barnes, J., O'Neill, M., Trudeau, M., and Neely, R.: Increase in background stratospheric
1272 aerosol observed with lidar at Mauna Loa Observatory and Boulder, Colorado, Geophys. Res. Lett., 36,
1273 <https://doi.org/10.1029/2009GL039008>, 2009.

1274 Holben, B. N., Eck, T. F., Slutsker, I., Tanre, D., Buis, J. P., Setzer, A., Vermote, E., Reagan, J. A.,
1275 Kaufman, Y. J., Nakajima, T., Lavenu, F., Jankowiak, I., and Smirnov, A.: AERONET - A federated
1276 instrument network and data archive for aerosol characterization, Remote Sens. Environ., 66, 1-16,
1277 [https://doi.org/10.1016/s0034-4257\(98\)00031-5](https://doi.org/10.1016/s0034-4257(98)00031-5), 1998.

1278 Hsu, N., Gautam, R., Sayer, A., Bettenhausen, C., Li, C., Jeong, M., Tsay, S.-C., and Holben, B.: Global
1279 and regional trends of aerosol optical depth over land and ocean using SeaWiFS measurements from
1280 1997 to 2010, Atmos. Chem. Phys., 12, 8037-8053, <https://doi.org/10.5194/acp-12-8037-2012>, 2012.

1281 Hsu, N., Jeong, M. J., Bettenhausen, C., Sayer, A., Hansell, R., Seftor, C., Huang, J., and Tsay, S. C.:
1282 Enhanced Deep Blue aerosol retrieval algorithm: The second generation, J. Geophys. Res.-Atmos., 118,
1283 9296-9315, <https://doi.org/10.1002/jgrd.50712>, 2013.

1284 Hsu, N., Lee, J., Sayer, A., Carletta, N., Chen, S. H., Tucker, C., Holben, B., and Tsay, S. C.: Retrieving
1285 near-global aerosol loading over land and ocean from AVHRR, J. Geophys. Res.-Atmos., 122, 9968-
1286 9989, <https://doi.org/10.1002/2017JD026932>, 2017.

1287 Hsu, N. C., Tsay, S.-C., King, M. D., and Herman, J. R.: Deep blue retrievals of Asian aerosol properties
1288 during ACE-Asia, Ieee T. Geosci. Remote., 44, 3180-3195, <https://doi.org/10.1109/tgrs.2006.879540>,
1289 2006.

1290 Hu, B., Zhang, X., Sun, R., and Zhu, X.: Retrieval of Horizontal Visibility Using MODIS Data: A Deep
1291 Learning Approach, Atmosphere-Basel, 10, <https://doi.org/10.3390/atmos10120740>, 2019.

1292 Hu, K., Kumar, K. R., Kang, N., Boiyo, R., and Wu, J.: Spatiotemporal characteristics of aerosols and
1293 their trends over mainland China with the recent Collection 6 MODIS and OMI satellite datasets, Environ.
1294 Sci. Pollut. R., 25, 6909-6927, <https://doi.org/10.1007/s11356-017-0715-6>, 2018.

1295 Husar, R. B., Husar, J. D., and Martin, L.: Distribution of continental surface aerosol extinction based on
1296 visual range data, Atmos. Environ., 34, 5067-5078, [https://doi.org/10.1016/s1352-2310\(00\)00324-1](https://doi.org/10.1016/s1352-2310(00)00324-1),
1297 2000.

1298 IPCC: Climate Change 2021: The Physical Science Basis, Cambridge University Press, New York, 2021.

1299 Ivanova, G., Ivanov, V., Kukavskaya, E., and Soja, A.: The frequency of forest fires in Scots pine stands
1300 of Tuva, Russia, Environ. Res. Lett., 5, 015002, <https://doi.org/10.1088/1748-9326/5/1/015002>, 2010.

1301 Kang, Y., Kim, M., Kang, E., Cho, D., and Im, J.: Improved retrievals of aerosol optical depth and fine
1302 mode fraction from GOCI geostationary satellite data using machine learning over East Asia, Isprs J.

1303 Photogramm., 183, 253-268, <https://doi.org/10.1016/j.isprsjprs.2021.11.016>, 2022.

1304 Kang, Y., Choi, H., Im, J., Park, S., Shin, M., Song, C.-K., and Kim, S.: Estimation of surface-level NO₂
1305 and O₃ concentrations using TROPOMI data and machine learning over East Asia, *Environ. Pollut.*, 288,
1306 117711, <https://doi.org/10.1016/j.envpol.2021.117711>, 2021.

1307 Karbowska, B. and Zembruski, W.: Fractionation and mobility of thallium in volcanic ashes after
1308 eruption of Eyjafjallajökull (2010) in Iceland, *B. Environ. Contam. Tox.*, 97, 37-43,
1309 <https://doi.org/10.1007/s00128-016-1831-6>, 2016.

1310 Kaufman, Y. J. and Boucher, O.: A satellite view of aerosols in the climate system, *Nature*, 419, 215-215,
1311 <https://doi.org/10.1038/nature01091>, 2002.

1312 Kim, D. H., Sohn, B. J., Nakajima, T., Takamura, T., Takemura, T., Choi, B. C., and Yoon, S. C.: Aerosol
1313 optical properties over east Asia determined from ground-based sky radiation measurements, *J. Geophys.*
1314 *Res-Atmos.*, 109, <https://doi.org/10.1029/2003jd003387>, 2004.

1315 Klett, J. D.: Lidar inversion with variable backscatter/extinction ratios, *Appl. Optics*, 24, 1638-1643,
1316 <https://doi.org/10.1364/AO.24.001638>, 1985.

1317 Koelemeijer, R., Homan, C., and Matthijsen, J.: Comparison of spatial and temporal variations of aerosol
1318 optical thickness and particulate matter over Europe, *Atmos. Environ.*, 40, 5304-5315,
1319 <https://doi.org/10.1016/j.atmosenv.2006.04.044>, 2006.

1320 Koschmieder, H.: Theorie der horizontalen Sichtweite, *Beitrage zur Physik der freien Atmosphäre*, 12,
1321 33-55, 1924.

1322 Krylov, A., McCarty, J. L., Potapov, P., Loboda, T., Tyukavina, A., Turubanova, S., and Hansen, M. C.:
1323 Remote sensing estimates of stand-replacement fires in Russia, 2002–2011, *Environ. Res. Lett.*, 9,
1324 105007, <https://doi.org/10.1088/1748-9326/9/10/105007>, 2014.

1325 Kulmala, M., Vehkamäki, H., Petäjä, T., Dal Maso, M., Lauri, A., Kerminen, V. M., Birmili, W., and
1326 McMurry, P. H.: Formation and growth rates of ultrafine atmospheric particles: A review of observations,
1327 *J. Aerosol Sci.*, 35, 143-176, <https://doi.org/10.1016/j.jaerosci.2003.10.003>, 2004.

1328 Kumm, M., De Moel, H., Salvucci, G., Viviroli, D., Ward, P. J., and Varis, O.: Over the hills and further
1329 away from coast: global geospatial patterns of human and environment over the 20th–21st centuries,
1330 *Environ. Res. Lett.*, 11, 034010, <https://doi.org/10.1088/1748-9326/11/3/034010>, 2016.

1331 Lapen, D. R. and Hayhoe, H. N.: Spatial analysis of seasonal and annual temperature and precipitation
1332 normals in southern Ontario, Canada, *J. Great Lakes Res.*, 29, 529-544, [https://doi.org/10.1016/s0380-1330\(03\)70457-2](https://doi.org/10.1016/s0380-1330(03)70457-2), 2003.

1334 Lee, L. A., Reddington, C. L., and Carslaw, K. S.: On the relationship between aerosol model uncertainty
1335 and radiative forcing uncertainty, *P. Natl. A. Sci.*, 113, 5820-5827,
1336 <https://doi.org/10.1073/pnas.1507050113>, 2016.

1337 Levy, R., Remer, L., Kleidman, R., Mattoo, S., Ichoku, C., Kahn, R., and Eck, T.: Global evaluation of
1338 the Collection 5 MODIS dark-target aerosol products over land, *Atmos. Chem. Phys.*, 10, 10399-10420,
1339 <https://doi.org/10.5194/acp-10-10399-2010>, 2010.

1340 Levy, R. C., Remer, L. A., Mattoo, S., Vermote, E. F., and Kaufman, Y. J.: Second-generation operational
1341 algorithm: Retrieval of aerosol properties over land from inversion of Moderate Resolution Imaging
1342 Spectroradiometer spectral reflectance, *J. Geophys. Res-Atmos.*, 112,
1343 <https://doi.org/10.1029/2006JD007811>, 2007.

1344 Levy, R. C., Mattoo, S., Munchak, L. A., Remer, L. A., Sayer, A. M., Patadia, F., and Hsu, N. C.: The
1345 Collection 6 MODIS aerosol products over land and ocean, *Atmos. Meas. Tech.*, 6, 2989-3034,
1346 <https://doi.org/10.5194/amt-6-2989-2013>, 2013.

1347 Levy, R. C., Mattoo, S., Sawyer, V., Shi, Y., Colarco, P. R., Lyapustin, A. I., Wang, Y., and Remer, L. A.:
1348 Exploring systematic offsets between aerosol products from the two MODIS sensors, *Atmos. Meas. Tech.*,
1349 11, 4073-4092, <https://doi.org/10.5194/amt-11-4073-2018>, 2018.

1350 Li, J., Garshick, E., Hart, J. E., Li, L., Shi, L., Al-Hemoud, A., Huang, S., and Koutrakis, P.: Estimation
1351 of ambient PM_{2.5} in Iraq and Kuwait from 2001 to 2018 using machine learning and remote sensing,
1352 *Environ. Int.*, 151, <https://doi.org/10.1016/j.envint.2021.106445>, 2021.

1353 Li, J., Carlson, B. E., Yung, Y. L., Lv, D., Hansen, J., Penner, J. E., Liao, H., Ramaswamy, V., Kahn, R.
1354 A., Zhang, P., Dubovik, O., Ding, A., Lacis, A. A., Zhang, L., and Dong, Y.: Scattering and absorbing
1355 aerosols in the climate system, *Nat. Rev. Earth. Environ.*, 3, 363-379, <https://doi.org/10.1038/s43017-022-00296-7>, 2022.

1357 Li, S., Chen, L., Huang, G., Lin, J., Yan, Y., Ni, R., Huo, Y., Wang, J., Liu, M., and Weng, H.: Retrieval
1358 of surface PM_{2.5} mass concentrations over North China using visibility measurements and GEOS-Chem
1359 simulations, *Atmos. Environ.*, 222, 117121, <https://doi.org/10.1016/j.atmosenv.2019.117121>, 2020.

1360 Li, Z., Lau, W. M., Ramanathan, V., Wu, G., Ding, Y., Manoj, M., Liu, J., Qian, Y., Li, J., and Zhou, T.:
1361 Aerosol and monsoon climate interactions over Asia, *Rev. Geophys.*, 54, 866-929,
1362 <https://doi.org/10.1002/2015RG000500>, 2016.

1363 Liao, H., Chang, W., and Yang, Y.: Climatic Effects of Air Pollutants over China: A Review, *Adv. Atmos.*
1364 *Sci.*, 32, 115-139, <https://doi.org/10.1007/s00376-014-0013-x>, 2015.

1365 Lin, J. T., van Donkelaar, A., Xin, J. Y., Che, H. Z., and Wang, Y. S.: Clear-sky aerosol optical depth over
1366 East China estimated from visibility measurements and chemical transport modeling, *Atmos. Environ.*,
1367 95, 258-267, <https://doi.org/10.1016/j.atmosenv.2014.06.044>, 2014.

1368 Liu, B., Ma, X., Ma, Y., Li, H., Jin, S., Fan, R., and Gong, W.: The relationship between atmospheric
1369 boundary layer and temperature inversion layer and their aerosol capture capabilities, *Atmos. Res.*, 271,
1370 <https://doi.org/10.1016/j.atmosres.2022.106121>, 2022.

1371 Mahowald, N. M., Ballantine, J. A., Feddema, J., and Ramankutty, N.: Global trends in visibility:
1372 implications for dust sources, *Atmos. Chem. Phys.*, 7, 3309-3339, <https://doi.org/10.5194/acp-7-3309-2007>, 2007.

1374 McNeill, V. F.: Atmospheric Aerosols: Clouds, Chemistry, and Climate, in: *Annu. Rev. Chem. Biomol.*,
1375 edited by: Prausnitz, J. M., *Annual Review of Chemical and Biomolecular Engineering*, 427-444,
1376 <https://doi.org/10.1146/annurev-chembioeng-060816-101538>, 2017.

1377 Mehta, M., Singh, R., Singh, A., and Singh, N.: Recent global aerosol optical depth variations and
1378 trends—A comparative study using MODIS and MISR level 3 datasets, *Remote Sens. Environ.*, 181,
1379 137-150, <https://doi.org/10.1016/j.rse.2016.04.004>, 2016.

1380 Mitra, R., Bajpai, A., and Biswas, K.: ADASYN-assisted machine learning for phase prediction of high
1381 entropy carbides, *Comp. Mater. Sci.*, 223, <https://doi.org/10.1016/j.commatsci.2023.112142>, 2023.

1382 Mortier, A., Gliß, J., Schulz, M., Aas, W., Andrews, E., Bian, H., Chin, M., Ginoux, P., Hand, J., and
1383 Holben, B.: Evaluation of climate model aerosol trends with ground-based observations over the last 2
1384 decades—an AeroCom and CMIP6 analysis, *Atmos. Chem. Phys.*, 20, 13355-13378,
1385 <https://doi.org/10.5194/acp-20-13355-2020>, 2020.

1386 Mukkavilli, S., Prasad, A., Taylor, R., Huang, J., Mitchell, R., Troccoli, A., and Kay, M.: Assessment of
1387 atmospheric aerosols from two reanalysis products over Australia, *Atmos. Res.*, 215, 149-164,
1388 <https://doi.org/10.1016/j.atmosres.2018.08.026>, 2019.

1389 Nagaraja Rao, C., Stowe, L., and McClain, E.: Remote sensing of aerosols over the oceans using AVHRR
1390 data Theory, practice and applications, *Int. J. Remote Sens.*, 10, 743-749,

1391 <https://doi.org/10.1080/01431168908903915>, 1989.

1392 Nakajima, T., Campanelli, M., Che, H., Estellés, V., Irie, H., Kim, S.-W., Kim, J., Liu, D., Nishizawa, T.,
1393 and Pandithurai, G.: An overview of and issues with sky radiometer technology and SKYNET, *Atmos.*
1394 *Meas. Tech.*, 13, 4195-4218, <https://doi.org/10.5194/amt-13-4195-2020>, 2020.

1395 NOAA, DOD, FAA, and USN: Automated Surface Observing System (ASOS) User's Guide, 1998.

1396 O'Reilly, J. E., Maritorena, S., Mitchell, B. G., Siegel, D. A., Carder, K. L., Garver, S. A., Kahru, M., and
1397 McClain, C.: Ocean color chlorophyll algorithms for SeaWiFS, *J. Geophys. Res.*, 103, 24937-24953,
1398 <https://doi.org/10.1029/98jc02160>, 1998.

1399 Pebesma, E. J.: Multivariable geostatistics in S: the gstat package, *Comput. Geosci.*, 30, 683-691,
1400 <https://doi.org/10.1016/j.cageo.2004.03.012>, 2004.

1401 Qiu, J. and Lin, Y.: A parameterization model of aerosol optical depths in China, *Acta. Meteorol. Sin.*,
1402 59, 368-372, <https://doi.org/10.11676/qxxb2001.039>, 2001.

1403 Ramanathan, V., Crutzen, P. J., Kiehl, J., and Rosenfeld, D.: Aerosols, climate, and the hydrological cycle,
1404 *Science*, 294, 2119-2124, <https://doi.org/10.1126/science.1064034>, 2001.

1405 Remer, L. A., Kleidman, R. G., Levy, R. C., Kaufman, Y. J., Tanre, D., Mattoo, S., Martins, J. V., Ichoku,
1406 C., Koren, I., Yu, H., and Holben, B. N.: Global aerosol climatology from the MODIS satellite sensors,
1407 *J. Geophys. Res-Atmos.*, 113, <https://doi.org/10.1029/2007jd009661>, 2008.

1408 Remer, L. A., Kaufman, Y. J., Tanre, D., Mattoo, S., Chu, D. A., Martins, J. V., Li, R. R., Ichoku, C.,
1409 Levy, R. C., Kleidman, R. G., Eck, T. F., Vermote, E., and Holben, B. N.: The MODIS aerosol algorithm,
1410 products, and validation, *J. Atmos. Sci.*, 62, 947-973, <https://doi.org/10.1175/jas3385.1>, 2005.

1411 Salomonson, V. V., Barnes, W. L., Maymon, P. W., Montgomery, H. E., and Ostrow, H.: MODIS:
1412 advanced facility instrument for studies of the Earth as a system, *Ieee T. Geosci. Remote.*, 27, 145-153,
1413 <https://doi.org/10.1109/36.20292>, 1987.

1414 Sawamura, P., Vernier, J. P., Barnes, J. E., Berkoff, T. A., Welton, E. J., Alados-Arboledas, L., Navas-
1415 Guzmán, F., Pappalardo, G., Mona, L., and Madonna, F.: Stratospheric AOD after the 2011 eruption of
1416 Nabro volcano measured by lidars over the Northern Hemisphere, *Environ. Res. Lett.*, 7, 34013-
1417 34021(34019), <https://doi.org/10.1088/1748-9326/7/3/034013>, 2012.

1418 Schutgens, N., Tsyro, S., Gryspeerdt, E., Goto, D., Weigum, N., Schulz, M., and Stier, P.: On the spatio-
1419 temporal representativeness of observations, *Atmos. Chem. Phys.*, 17, 9761-9780,
1420 <https://doi.org/10.5194/acp-17-9761-2017>, 2017.

1421 Singh, A., Mahata, K. S., Rupakheti, M., Junkermann, W., Panday, A. K., and Lawrence, M. G.: An
1422 overview of airborne measurement in Nepal—Part 1: Vertical profile of aerosol size, number, spectral
1423 absorption, and meteorology, *Atmos. Chem. Phys.*, 19, 245-258, [https://doi.org/10.5194/acp-19-245-](https://doi.org/10.5194/acp-19-245-2019)
1424 [2019](https://doi.org/10.5194/acp-19-245-2019), 2019.

1425 Smirnov, A., Holben, B., Slutsker, I., Giles, D., McClain, C., Eck, T., Sakerin, S., Macke, A., Croot, P.,
1426 and Zibordi, G.: Maritime aerosol network as a component of aerosol robotic network, *J. Geophys. Res-*
1427 *Atmos.*, 114, <https://doi.org/10.1029/2008JD011257>, 2009.

1428 Streets, D. G., Yan, F., Chin, M., Diehl, T., Mahowald, N., Schultz, M., Wild, M., Wu, Y., and Yu, C.:
1429 Anthropogenic and natural contributions to regional trends in aerosol optical depth, 1980–2006, *J.*
1430 *Geophys. Res-Atmos.*, 114, <https://doi.org/10.1029/2008JD011624>, 2009.

1431 Sun, E., Xu, X., Che, H., Tang, Z., Gui, K., An, L., Lu, C., and Shi, G.: Variation in MERRA-2 aerosol
1432 optical depth and absorption aerosol optical depth over China from 1980 to 2017, *J. Atmos. Sol-Terr.*
1433 *Phy.*, 186, 8-19, <https://doi.org/10.1016/j.jastp.2019.01.019>, 2019.

1434 Sun, Y. and Zhao, C.: Influence of Saharan dust on the large-scale meteorological environment for

1435 development of tropical cyclone over North Atlantic Ocean Basin, *J. Geophys. Res-Atmos.*, 125,
1436 e2020JD033454, <https://doi.org/10.1029/2020JD033454>, 2020.

1437 Teixeira, A.: Classification and regression tree, *Rev. Mal. Respir.*, 21, 1174-1176,
1438 [https://doi.org/10.1016/S0761-8425\(04\)71596-X](https://doi.org/10.1016/S0761-8425(04)71596-X), 2004.

1439 Tian, X., Tang, C., Wu, X., Yang, J., Zhao, F., and Liu, D.: The global spatial-temporal distribution and
1440 EOF analysis of AOD based on MODIS data during 2003-2021, *Atmos. Environ.*, 302,
1441 <https://doi.org/10.1016/j.atmosenv.2023.119722>, 2023.

1442 Tupper, A., Oswalt, J. S., and Rosenfeld, D.: Satellite and radar analysis of the volcanic-cumulonimbi at
1443 Mount Pinatubo, Philippines, 1991, *J. Geophys. Res-Atmos.*, 110,
1444 <https://doi.org/10.1029/2004JD005499>, 2005.

1445 van der Veer, G., Voerkelius, S., Lorentz, G., Heiss, G., and Hoogewerff, J. A.: Spatial interpolation of
1446 the deuterium and oxygen-18 composition of global precipitation using temperature as ancillary variable,
1447 *Journal of Geochemical Exploration*, 101, 175-184, <https://doi.org/10.1016/j.gexplo.2008.06.008>, 2009.

1448 Vernier, J. P., Thomason, L. W., Pommereau, J. P., Bourassa, A., Pelon, J., Garnier, A., Hauchecorne, A.,
1449 Blanot, L., Trepte, C., and Degenstein, D.: Major influence of tropical volcanic eruptions on the
1450 stratospheric aerosol layer during the last decade, *Geophys. Res. Lett.*, 38,
1451 <https://doi.org/10.1029/2011GL047563>, 2011.

1452 Wang, K., Dickinson, R. E., and Liang, S.: Clear Sky Visibility Has Decreased over Land Globally from
1453 1973 to 2007, *Science*, 323, 1468-1470, <https://doi.org/10.1126/science.1167549>, 2009.

1454 Wang, K. C., Dickinson, R. E., Su, L., and Trenberth, K. E.: Contrasting trends of mass and optical
1455 properties of aerosols over the Northern Hemisphere from 1992 to 2011, *Atmos. Chem. Phys.*, 12, 9387-
1456 9398, <https://doi.org/10.5194/acp-12-9387-2012>, 2012.

1457 Wei, J., Li, Z., Peng, Y., and Sun, L.: MODIS Collection 6.1 aerosol optical depth products over land and
1458 ocean: validation and comparison, *Atmos. Environ.*, 201, 428-440,
1459 <https://doi.org/10.1016/j.atmosenv.2018.12.004>, 2019.

1460 Wei, J., Li, Z., Sun, L., Peng, Y., Liu, L., He, L., Qin, W., and Cribb, M.: MODIS Collection 6.1 3 km
1461 resolution aerosol optical depth product: Global evaluation and uncertainty analysis, *Atmos. Environ.*,
1462 240, 117768, <https://doi.org/10.1016/j.atmosenv.2020.117768>, 2020.

1463 Welton, E. J., Campbell, J. R., Berkoff, T. A., Spinhirne, J. D., and Starr, D. O.: The micro-pulse lidar
1464 network (MPLNET), *Frontiers in Optics*, <https://doi.org/10.1364/fio.2003.mk2>, 2002.

1465 Winker, D. M., Tackett, J. L., Getzewich, B. J., Liu, Z., Vaughan, M. A., and Rogers, R. R.: The global
1466 3-D distribution of tropospheric aerosols as characterized by CALIOP, *Atmos. Chem. Phys.*, 13, 3345-
1467 3361, <https://doi.org/10.5194/acp-13-3345-2013>, 2013.

1468 Winker, D. M., Vaughan, M. A., Omar, A., Hu, Y., Powell, K. A., Liu, Z., Hunt, W. H., and Young, S. A.:
1469 Overview of the CALIPSO Mission and CALIOP Data Processing Algorithms, *J. Atmos. Ocean. Tech.*,
1470 26, 2310-2323, <https://doi.org/10.1175/2009jtecha1281.1>, 2009.

1471 Wu, J., Luo, J., Zhang, L., Xia, L., Zhao, D., and Tang, J.: Improvement of aerosol optical depth retrieval
1472 using visibility data in China during the past 50years, *J. Geophys. Res-Atmos.*, 119, 13370-13387,
1473 <https://doi.org/10.1002/2014jd021550>, 2014.

1474 Xia, X., Che, H., Zhu, J., Chen, H., Cong, Z., Deng, X., Fan, X., Fu, Y., Goloub, P., and Jiang, H.: Ground-
1475 based remote sensing of aerosol climatology in China: Aerosol optical properties, direct radiative effect
1476 and its parameterization, *Atmos. Environ.*, 124, 243-251,
1477 <https://doi.org/10.1016/j.atmosenv.2015.05.071>, 2016.

1478 Yang, X., Zhao, C., Yang, Y., and Fan, H.: Long-term multi-source data analysis about the characteristics

1479 of aerosol optical properties and types over Australia, *Atmos. Chem. Phys.*, 21, 3803-3825,
1480 <https://doi.org/10.5194/acp-21-3803-2021>, 2021a.

1481 Yang, X., Zhao, C., Yang, Y., Yan, X., and Fan, H.: Statistical aerosol properties associated with fire
1482 events from 2002 to 2019 and a case analysis in 2019 over Australia, *Atmos. Chem. Phys.*, 21, 3833-
1483 3853, <https://doi.org/10.5194/acp-21-3833-2021>, 2021b.

1484 Yang, X., Wang, Y., Zhao, C., Fan, H., Yang, Y., Chi, Y., Shen, L., and Yan, X.: Health risk and disease
1485 burden attributable to long-term global fine-mode particles, *Chemosphere*, 287,
1486 <https://doi.org/10.1016/j.chemosphere.2021.132435>, 2022.

1487 Yang, Y., Ge, B., Chen, X., Yang, W., Wang, Z., Chen, H., Xu, D., Wang, J., Tan, Q., and Wang, Z.:
1488 Impact of water vapor content on visibility: Fog-haze conversion and its implications to pollution control,
1489 *Atmos. Res.*, 256, <https://doi.org/10.1016/j.atmosres.2021.105565>, 2021c.

1490 Yoon, J., Burrows, J., Vountas, M. v., von Hoyningen-Huene, W., Chang, D., Richter, A., and Hilboll, A.:
1491 Changes in atmospheric aerosol loading retrieved from space-based measurements during the past decade,
1492 *Atmos. Chem. Phys.*, 14, 6881-6902, <https://doi.org/10.5194/acp-14-6881-2014>, 2014.

1493 Yoon, J., Pozzer, A., Chang, D. Y., Lelieveld, J., Kim, J., Kim, M., Lee, Y., Koo, J.-H., Lee, J., and Moon,
1494 K.: Trend estimates of AERONET-observed and model-simulated AOTs between 1993 and 2013, *Atmos.*
1495 *Environ.*, 125, 33-47, <https://doi.org/10.1016/j.atmosenv.2015.10.058>, 2016.

1496 Zhang, S., Wu, J., Fan, W., Yang, Q., and Zhao, D.: Review of aerosol optical depth retrieval using
1497 visibility data, *Earth-Sci. Rev.*, 200, 102986, <https://doi.org/10.1016/j.earscirev.2019.102986>, 2020.

1498 Zhang, Z., Wu, W., Wei, J., Song, Y., Yan, X., Zhu, L., and Wang, Q.: Aerosol optical depth retrieval from
1499 visibility in China during 1973-2014, *Atmos. Environ.*, 171, 38-48,
1500 <https://doi.org/10.1016/j.atmosenv.2017.09.004>, 2017.

1501 Zhao, A. D., Stevenson, D. S., and Bollasina, M. A.: The role of anthropogenic aerosols in future
1502 precipitation extremes over the Asian Monsoon Region, *Clim. Dynam.*, 52, 6257-6278,
1503 <https://doi.org/10.1007/s00382-018-4514-7>, 2019.

1504